Available online at www.sciencedirect.com
ScienceDirect
Coordination Chemistry Reviews 253 (2009) 250–267
COORDINATION CHEMISTRY REVIEWS
www.elsevier.com/locate/ccr

Review

Hydrotalcites and their role in coordination of anions in Bayer liquors: Anion binding in layered double hydroxides

Sara J. Palmer, Ray L. Frost*, Tai Nguyen

Inorganic Materials Research Program, School of Physical and Chemical Sciences, Queensland University of Technology, GPO Box 2434, Brisbane Queensland 4001, Australia

Received 15 October 2007; accepted 8 January 2008
Available online 17 January 2008

Contents

1. Bauxite refinery residues (red mud) 251
 1.1. Bayer process – origin of red mud 251
 1.2. Components of red mud 251
  1.2.1. Iron oxides 251
  1.2.2. Silica minerals 253
 1.3. Surface chemistry 254
 1.4. Removal of trace metals from solution 255
 1.5. Acid neutralising capacity (ANC) 255
2. Seawater neutralised bauxite refinery residues 256
 2.1. Introduction 256
 2.2. Reaction mechanism 256
 2.3. Formation of hydrotalcite 256
 2.4. Adsorption of anions on the surface of neutralised red mud 257
3. Layered double hydroxides (LDH) 257
 3.1. Introduction 257
 3.2. Preparation of LDHs 258
 3.3. Anionic exchange 259
 3.4. Reformation of hydrotalcites 260
 3.5. Characterisation of LDHs 260
  3.5.1. Vibrational spectroscopy – infrared (IR) and Raman spectroscopy 260
  3.5.2. TGA/DTG/DTA 263
  3.5.3. X-ray diffraction (XRD) 263
 3.6. LDHs in the alumina industries 264
4. Summary 264
 Acknowledgements 264
 References 264

Abstract

Bauxite refinery residues (red mud) are derived from the Bayer process by the digestion of crushed bauxite in concentrated caustic at elevated temperatures and pressures. Following the recovery of the valuable alumina containing portion, there remains an alkaline residue consisting primarily of iron oxides, aluminium oxides, silica oxides, titanium oxides and trace heavy metals. This slurry residue, if untreated, is unsuitable for discharge directly into the environment and is usually stored in holding dams. The liquid portion has the potential for discharge, but requires pre-treatment before this can occur. Seawater neutralisation of the solid residue is one such treatment which has been employed in recent years. This process facilitates a significant reduction in pH and dissolved metal concentrations, through the precipitation of hydrotalcite-like compounds and some other Mg, Ca, and Al hydroxide and carbonate minerals. The hydrotalcite-like compounds, precipitated during seawater neutralisation,

* Corresponding author.
E-mail address: r.frost@qut.edu.au (R.L. Frost).

doi:10.1016/j.ccr.2008.01.012

also remove oxy-anions of transition metals through a combination of intercalation and adsorption of the anionic species on the external surfaces, where small anions are intercalated while larger organic molecules are adsorbed.

Layered double hydroxides (LDHs) have been investigated for many years as host materials for a range of anion exchange intercalation reactions. The lamellar structure of LDHs can be used for the controlled addition or removal of a variety of species, both organic and inorganic. This is achieved through their ability to adjust the separation of the hydroxide layers, and the reactivity of the interlayer region. The high affinity of hydrotalcites for carbonate anions means that it cannot be reversibly exchanged and so prevents its use as an anion exchange material. However, carbonate can be removed by thermal decomposition, evolving CO_2. The resultant material adsorbs anions when placed in solution and reverts to the hydrotalcite structure. Significant advances have been made recently on the characterisation of these materials, including structural studies on the mechanism of intercalation.

Keywords: Bayer process; Seawater neutralisation; Hydrotalcites; Vanadate; Molybdite; Layered double hydroxides

1. Bauxite refinery residues (red mud)

1.1. Bayer process – origin of red mud

Bauxite refinery residues are derived from the Bayer process, summarised in Eqs. (1), (2), and (3) [1], by the digestion of crushed bauxite in concentrated caustic (NaOH) at elevated temperatures. Digestion temperatures are dependent on the quantity of gibbsite (γ-$Al(OH)_3$), boehmite (γ-Al(O)OH), and diaspore (α-Al(O)OH) present in the bauxite ore. Bauxites containing predominantly gibbsite require lower digestion temperatures (145–175 °C), while those with high boehmite and diaspore require stronger caustic concentrations and temperatures (245–275 °C) [2]. The process results in the dissolution of gibbsite ($Al(OH)_3$) and boehmite as sodium aluminate, while the remaining insoluble residue (45% liquor and 55% solid mud), known widely as red mud, is removed by means of flocculation and decantation [1,3]. The exact composition of the fine textured residue depends on the initial type of bauxite [4]. Roughly 1.0–1.5 tonnes of red mud residue is produced for every tonne of alumina produced [5], therefore millions of tonnes of red mud is produced annually. The liquor is strongly alkaline (pH ranging from 10 to 13) [6–8] and requires neutralisation to a pH below 9, with an optimum pH value of 8.5–8.9 [9–11], before becoming environmentally benign. The liquor also contains relatively high concentrations of aluminium and a variety of anionic species including oxy-anions of transition metals. Many of these species can be detrimental to the environment [9] and therefore must be removed prior to disposal. Bayer process red mud and their environmental applications have received substantial research [12–16].

$$\text{Extraction}: \begin{array}{l} Al(OH)_{3(s)} + NaOH_{(aq)} \rightarrow Na^+Al(OH)_{4(aq)}{}^- \text{ (Gibbsitic bauxite)} \\ AlO(OH)_{(s)} + NaOH_{(aq)} + H_2O \xrightarrow{\text{Insoluble residue is removed}} Na^+Al(OH)_{4(aq)}{}^- \text{ (Boehmitic bauxite)} \end{array} \quad (1)$$

$$\text{Precipitation}: Na^+Al(OH)_{4(aq)}{}^- \rightarrow Al(OH)_{3(s)} + NaOH_{(aq)} \quad (2)$$

$$\text{Calcination}: 2Al(OH)_{3(s)} \rightarrow Al_2O_{3(s)} + 3H_2O_{(g)} \quad (3)$$

Red mud varies in physical, chemical, and mineralogical properties due to differing bauxite ore sources and refining processes employed [17–19]. Table 1 demonstrates the variability of bauxites mined in different areas of the world. The general consensus of the composition of red mud is that it is largely composed of iron oxides, primarily hematite (Fe_2O_3), and goethite ((FeOOH), boehmite (AlOOH), other aluminium hydroxides, calcium oxides, titanium oxides (anatase and rutile), and aluminosilicate minerals (sodalite) [3,11,17,19]. Charged lime species may also be present in the form of calcium carbonate ($CaCO_3$), $3CaO{\cdot}Al_2O_3{\cdot}6H_2O$, various forms of calcium phosphate (carbonate or hydroxyapatite), as well as the formation of perovskite ($CaTiO_3$) and/or kassite ($CaTi_2O_4(OH)_2$) at high bauxite digestion temperatures [3]. These minerals are the chemically stable end products of bauxite formation and refining, and are the components responsible for the high surface reactivity of red muds [1,3,11,17,20].

1.2. Components of red mud

1.2.1. Iron oxides

In general, the solubility of Fe^{III} oxides is low, while Fe^{II} oxides are sparingly soluble. In the pH range 4–10 the level of total Fe in solution is $<10^{-6}$ M [26]. Iron oxides dissolve slowly over a wide pH range. The solubility diagram, Fig. 1, of hematite and goethite indicates that the iron oxides appear to have minimum solubility around pH 7–8, which is around the point of zero charge (PZC). As iron oxides are amphoteric, they dissolve in acid media to form cationic hydroxo species and in basic media to form anionic hydroxo species, Table 2. The solubility of the iron oxides rises at pH values greater and lower than 7–8.

The particle size of the solid will affect solubility, where crystals <1 μm may increase solubility due to the high surface area. This occurs because it is the surface properties, especially the surface free energy, rather than the properties of the bulk solution, that govern the dissolution behaviour. Surface free energies of iron oxides are relatively high, therefore particle sizes will have a noticeable effect on the solubility of the compound.

Numerous measurements of the solubility products of goethite have been made [27–30], but there are fewer for hematite. There are often discrepancies (up to three orders of magnitude) between the results of different authors, probably

Table 1
Mineralogy of some typical bauxites [21–25]

Minerals	Weipa [21]	Darling range [22]	Guinea Boké [21]	Jamaica [22]	India [23]	Hungary Iszkaszentgyogy [24]	Greece [25]
Gibbsite, $Al(OH)_3$	58.3	51.1	71.9	64.7	59.2	24.5	0
Boehmite, AlO(OH)	12.5	0.4	14.4	3.6	7.8	30	3.0
Diaspore, AlO(OH)	0.2	0.5	0.3	0.2	1.2	1.5	60.0
Kaolin, $A1_2O_3{\cdot}2SiO_2{\cdot}2H_2O$	10.3	6.5	2.3	3.4	5.6	12.7	3.0
Quartz, SiO_2	Trace	17.4	0	0.5	1.4	0.5	0
Hematite, Fe_2O_3	10.6	7.2	2.6	15.8	10.7	5.2	21.0
Goethite, FeO(OH)	3.9	9.5	2.4	5.3	6.2	13.8	4.0
Anatase, TiO_2	2.0	1.0	2.7	2.2	6.0	1.8	3.0
Rutile, TiO_2	0.7	0	0.8	0.5	0.5	0.6	0
P_2O_5	0.1	NR	0	0.7	NR	NR	NR
CaO	0.1	0	0.1	0.9	NR	0.6	0.7
	98.7	93.7	97.5	97.8	98.6	91.2	94.7

NR, not reported.

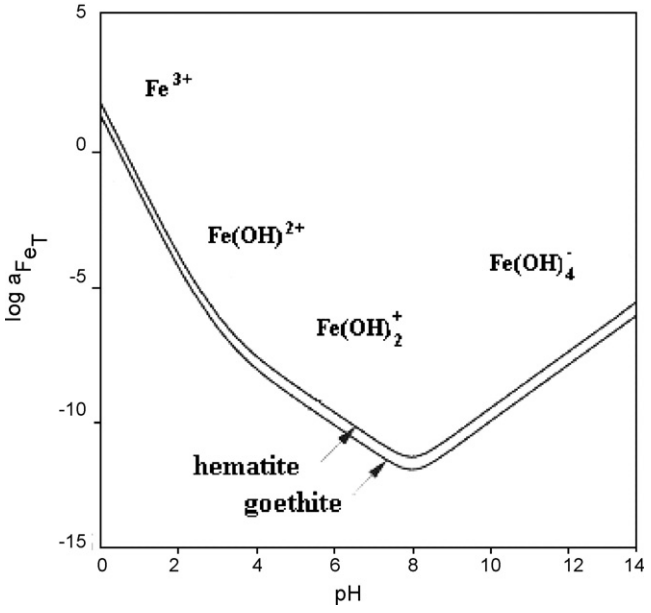

Fig. 1. Solubilities of goethite and hematite as a function of pH [26].

due to some of the properties of iron oxides, especially particle size and crystallinity. Researchers in the aluminium industry have investigated the solubility of goethite in sodium aluminate solutions and NaOH solutions. Basu [31], reported that the solubility of goethite in sodium aluminate solutions was close to zero at room temperature and increased exponentially as the temperature rose above 100 °C. The dissolution reactions of goethite are given in Eqs. (4) and (5). The solubility of hematite was found to rise with rising hydroxide concentrations [32], and the alkali hydroxide solution it was present in (NaOH > KOH > LiOH) [33]. The dissociation of hematite is described by Eq. (6). In very concentrated solutions of NaOH, ion pairs form between $Fe(OH)_4^-$ and the cation, which increased the solubility of hematite when temperatures are greater then 200 °C.

Table 2
Equilibria for the iron hydroxo complexes [26]

Equilibrium reaction	
$Fe(OH)_2 + OH^-$	$\rightarrow Fe(OH)_3^-$
$Fe(OH)_2 + 2OH^-$	$\rightarrow Fe(OH)_4^{2-}$
$Fe(OH)_3 + H^+$	$\rightarrow Fe(OH)_2^+ + H_2O$
$Fe(OH)_3 + 2H^+$	$\rightarrow FeOH^{2+} + 2H_2O$
$Fe(OH)_3 + OH^-$	$\rightarrow Fe(OH)_4^-$
$2Fe(OH)_3 + 4H^+$	$\rightarrow Fe_2(OH)_2^{4+} + 4H_2O$
α-$FeOOH + H_2O$	$\rightarrow FeOH_3^0$
α-$FeOOH + H_2O + OH^-$	$\rightarrow Fe(OH)_4^-$
0.5α-$Fe_2O_3 + 2.5H_2O$	$\rightarrow Fe(OH)_4^- + H^+$

$$FeOOH + H_2O \leftrightarrow Fe^{3+} + 3OH^- \quad (4)$$

$$FeOOH + 3H^+ \leftrightarrow Fe^{3+} + 2H_2O \quad (5)$$

$$0.5\alpha Fe_2O_3 + 2.5H_2O \rightarrow Fe(OH)_4^- + H^+ \quad (6)$$

The surface hydroxyl groups (whether they arise from the adsorption of water or from structural OH) are the chemically reactive entities at the surface of the solid in an aqueous environment. They possess a double pair of electrons together with a dissociable hydrogen atom which enables them to react with both acids and bases, therefore making iron oxides amphoteric (Eqs. (7) and (8)).

$$\equiv FeOH_2^+ \leftrightarrow FeOH + H^+ \quad (7)$$

$$\equiv FeOH \leftrightarrow FeO^- + H^+ \quad (8)$$

where ≡ denotes the surface.

The surface groups can be replaced by silane groups [34], or by titanate groups [35], shown in Eq. (9).

$$ROTi(-OR')_3 + \equiv OH \rightarrow \equiv OTi(OR')_3 + ROH \quad (9)$$

where R and R′ are alkly groups and ≡ represents the oxide surface.

Crystallographic considerations indicate that the surface hydroxyl groups may be coordinated to one (singly), two (doubly), or three (triply) underlying Fe atoms, Fig. 2. The overall density of these groups depends on both the crystal structure and on the extent of development of the different crystal faces. Therefore, the density of the hydroxyl groups depends on the oxide and its crystal morphology. The most reactive groups are singly coor-

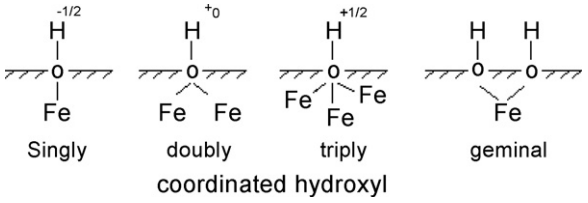

Fig. 2. Singly, doubly, triply coordinated and geminal surface hydroxyl groups on iron oxides [26].

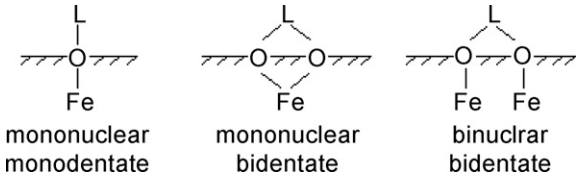

Fig. 3. Modes of ligand coordination to the iron oxide surface [26].

dinated, with total hydroxyl densities between 8 and 16 nm^{-2} OH [36]. Due to the differences in the number of underlying Fe atoms that are coordinated to the surface functional groups, the acidity and hence, the reactivity of the different types of hydroxyl groups should vary. Adsorption studies appear to indicate doubly coordinated surface hydroxyls on goethite and hematite are inert over a wide pH range [37–40]. Adsorption of ions on iron oxides is considered to involve only singly coordinated surface groups. The density of surface functional groups on various iron oxides has been measured by such techniques as acid/base titration [41,42], BET treatment of water vapour isotherms [43], D_2O or titanium exchange [44], and by reactions with the adsorbing species such as fluoride, phosphate or oxalate [42,45].

The adsorption process involves the interaction of the adsorbing species, the adsorbate, with the surface hydroxyl groups on the iron oxide, the absorbent. The oxygen donor atom of the surface hydroxyl group can interact with protons, whereas the underlying metal ion acts as a Lewis acid and exchanges the OH group for other ligands to form surface complexes. Adsorption of simple inorganic anions, oxy-anions and organic ions on iron oxides has been widely investigated [46–54]. Anions are ligands, i.e. they posses one or more atoms with a lone pair of electrons and can therefore function as the donor in a coordinate bond. Adsorption of anions on iron oxides can occur either specifically or non specifically. Specific adsorption involves the replacement of the surface hydroxyl group by the adsorbing ligand, L, Eqs. (10) and (11). It involves the direct coordination of the adsorbing species to the surface metal atom of the solid. It is also termed chemisorption, inner sphere adsorption, and in the case of ligands, ligand exchange. Specifically adsorbing ions modify the surface charge on the oxide and hence, cause a shift in the PZC (discussed in surface chemistry of red mud). They are usually tightly bound and are not easily displaced. Anions that adsorb specifically on iron oxides include phosphate, silicate, selenate, arsenate, chloride, fluoride, citrate, and oxalate [26].

$$\equiv FeOH + L^- \rightarrow FeL + OH^- \quad (10)$$

$$\equiv (FeOH)_2 + L^- \rightarrow Fe_2L^+ + 2OH^- \quad (11)$$

where ≡ denotes the surface.

Anion adsorption at any pH increases with increasing concentration of the adsorbing species. Adsorption is at a maximum at low pH and decreases with increasing pH except for silicate [55]. The decrease in adsorption at increasing pHs is a result of a decrease in the number of $FeOH_2^+$ groups present (Fig. 3).

Adsorption of cations on iron oxides are also specific and non specific, where the trivalent cations (Al^{3+}) appear to adsorb as surface hydroxo species, Eq. (12).

$$\equiv FeOH + Al^{3+} + H_2O \leftrightarrow \equiv Fe{-}O{-}AlOH^+ + 2H^+ \quad (12)$$

Cation adsorption on iron oxides is initially rapid, but adsorption of trace metals can continue to increase over days with long reaction times being needed to reach equilibrium. Adsorption of Ni, Zn, and Cd on goethite rose as the reaction time was extended from 2 h to 42 days [56]. Adsorption of aluminium on iron oxides is of interest due to the environmental effect of high levels of Al in waters and soils. Adsorption on goethite takes place over the pH range 3–8.5 [57,58]. The data fit the adsorption model with two monodentate surface hydroxo-complexes (Fe–$OAlOH^+$ and $FeOAl(OH)_2$) which formed successively as the pH increased. Desorption of aluminium from goethite is extremely slow and adsorption is only partly reversible.

1.2.2. Silica minerals

The main impurities in bauxites are compounds of silica, iron, and titanium. Silica is present as kaolinite ($Al_2O_3{\cdot}2SiO_2{\cdot}2H_2O$) and halloysite ($Al_2O_3{\cdot}2SiO_2{\cdot}3H_2O$) [2]. Silica, in the form of quartz, is not perceptibly attacked during low temperature digestion in the Bayer process, however, silica combined as clay (reactive silica) dissolves in caustic soda. Quartz can be attacked during high temperature digestion, however. It then reacts with soda and alumina in solution and partly precipitates as sodium aluminosilicate (DSP) or sodalite, Eq. (13) [21,59,60]. The dissolved silica precipitates as sodium aluminosilicate scale throughout the alumina refinery [61], where the exact nature and location of the scale depends on the conditions of formation [62]. Bayer sodalite has the general composition: $(3(Na_2O{\cdot}Al_2O_3{\cdot}2SiO_2{\cdot}nH_2O){\cdot}Na_2X)$ where n ranges from 0 to 2 and X represents CO_3^{2-}, SO_4^{2-}, $2OH^-$, $2Cl^-$, or a mixture of all, depending on the impurities within the digested liquor [3,17]. The process of formation is described by Eq. (14). Under normal conditions, DSP is discarded with red mud.

$$Al_2O_3{\cdot}2SiO_2 + NaOH \rightarrow Na_2SiO_3 \quad (13)$$

$$6SiO_3^{2-} + 6Al(OH)_4^- + 6Na^+ + 2NaX \rightarrow Na_8[AlSiO_4]_6X_2 \cdot nH_2O_{(s)}\ \text{(sodium aluminosilicate)} + (6-n)H_2O + 12OH^- \quad (14)$$

where, X can be $\frac{1}{2}CO_3^{2-}$, $\frac{1}{2}SO_4^{2-}$, $2OH^-$, $2Cl^-$.

Cancrinite and sodalite are common sodium aluminosilicate compounds that form in strongly caustic alkaline aqueous solutions. Cancrinite is defined as belonging to the hexagonal crystal system with ABAB layer type packing. Large channels as well as a series of smaller cages run parallel to the

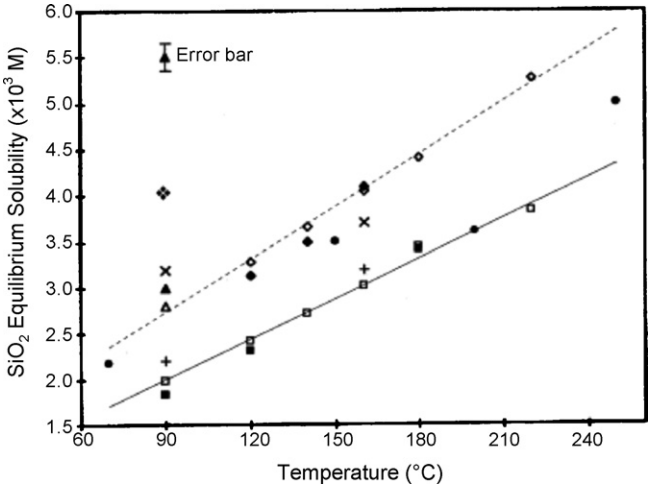

Fig. 4. The SiO_2 equilibrium solubility of sodalite and cancrinite formed under different conditions [68].

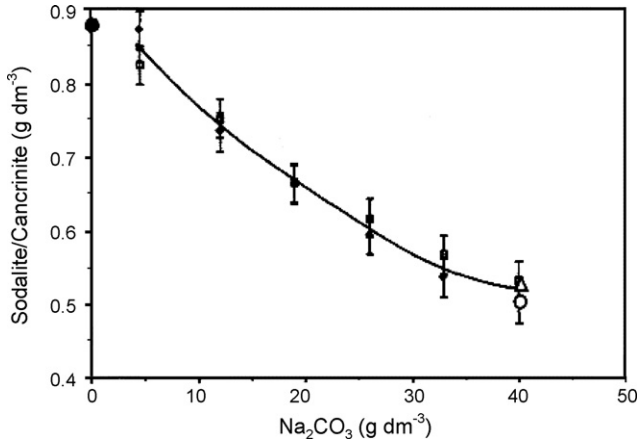

Fig. 5. Aluminosilicate solubility in a synthetic Bayer solution as a function of Na_2CO_3 concentration at 90 °C [75].

z-axis [63]. Cancrinite has characteristic infrared frequencies at 1095, 1035, and 1000 cm^{-1} attributed to the asymmetric stretch, ν(Al–O–Si) of the aluminosilicate framework [64], and at 690, 630, and 560 cm^{-1} for the symmetric stretch of the aluminosilicate framework [65]. Sodalite has a general cubic crystal system with ABC layer packing creating a network of large cages rather then channels, like that of cancrinite. Sodalite has characteristic infrared spectra at 1000 cm^{-1} attributed to the asymmetric stretch of the Al–O–Si framework, with symmetric frequencies located at 737, 713, and 668 cm^{-1} [65].

Silica solubility has been shown to increase with increasing sodium hydroxide and alumina concentrations [66]. There is some disagreement as to the effect of temperature on silica solubility. Ostap [66], Breuer et al. [67], and Barnes et al. [68], reported increasing solubility with increasing temperature for Bayer solutions. Barnes et al. [68], investigated the solubility of sodalite and cancrinite (expressed in terms of SiO_2 concentration) with increased temperature, Fig. 4. Sodalite had increased equilibrium SiO_2 solubility then cancrinite at all temperatures [68]. However, Oku et al. [69], reported no temperature dependence, up to 150 °C, in the desilication rate of Bayer liquors. Ni et al. [70], measured the solubility of sodium aluminosilicate solutions, where no sodium carbonate (Na_2CO_3) has been added, and found that sodium aluminosilicate solubility increases with increasing alkali concentration, Fig. 5. The presence of Na_2CO_3 in solution decreases the solubility of both cancrinite and sodalite.

Studies have shown that sodalite transforms to cancrinite ($Na_6Ca_{1.5}Al_6Si_6O_{24}(CO_3)_{1.6}$) over time [69,71], however variations exist in literature in regards to the rate of transformation. The mechanisms and kinetics of sodalite and cancrinite formation have been reported in literature [72–74]. The presence of Na_2CO_3 in synthetic liquor causes a decrease in the rate of transformation of sodalite to cancrinite.

1.3. Surface chemistry

The surface chemistry of red mud particles is extremely complex due to the variable red mud slurries. Difficulties also arise in the determination of the chemical composition of the red mud surface due to the thin surface layer of red mud, 50 Å to 1 μm [3]. However, it is well known that the majority of the minerals and oxides found in red mud demonstrate acid/base type behaviour in aqueous solutions [76,77], and therefore it is expected that red mud particles will exhibit similar behaviour. The acid/base properties of the particles are believed to be due to the surface hydroxyl groups [3]. The specific surface area and adsorption capacity for protons of acid treated red mud is 20.7 $m^2\ g^{-1}$ and 2.5×10^{-2} mol g^{-1}, respectively [78]. Santona et al. [19], found the surface area of red mud varies for non-treated and acid neutralised samples, 18.9 and 25.2 $m^2\ g^{-1}$. The increase in surface area after acid neutralisation was attributed to the partial dissolution of red mud species, possibly cancrinte which showed a 9 wt.% decrease after neutralisation [19].

Chevedov et al. [3], studied the surface properties of red mud by means of potentiometric titration [79,80], and found that three zones, Fig. 6, existed due to different mechanisms occurring at the red mud surface. Red mud particles can con-

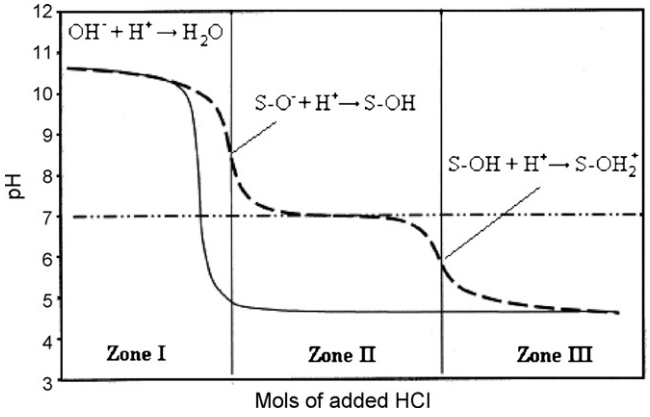

Fig. 6. Titration curves of red mud slurry (dotted line) and caustic solution (solid line) [3].

sume H^+ without a change in pH (Zone I) due to the presence of free hydroxide ions (OH^-) reacting with protons (Eq. (15)) more readily then the ionised surface hydroxyl groups. However, small amounts of surface hydroxyl groups were found to protonate in this zone. The inflection point between Zones I and II represents red mud particles in basic aqueous solutions carrying ionised surface hydroxyl groups ($S–O^-$) consuming protons, Eq. (16). At neutral pH, Zone II, all free hydroxide ions are consumed and protons added to the slurry are then consumed by surface hydroxyl groups resulting in a constant pH. Once all of the surface hydroxyl groups have been neutralised, end of Zone II, accumulation of protons in solution causes the second rapid drop in pH, Zone III.

$$\text{Zone I}: \quad \begin{matrix} OH^- + H^+ \rightarrow H_2O \quad \text{(primary reaction)} \\ S–O^- + H^+ \rightarrow S–OH \end{matrix} \tag{15}$$

$$\text{Zone II}: \quad S–O^- + H^+ \rightarrow S–OH \tag{16}$$

$$\text{Zone III}: \quad S–OH + H^+ \rightarrow S–OH_2{}^+ \tag{17}$$

The amount of surface hydroxyl groups is roughly proportional to the reactive silica content in the original bauxite [81]. Sodalite is a zeolite-type compound with a high surface area of exposed oxygen atoms that react with protons [3]. Estimates for the number of surface hydroxyl groups on red mud obtained by Chevedov et al. [3], were two orders of magnitude higher then the average values obtained for metal oxides [82], suggesting that a high level of sodalite on the surface of red mud was present.

The surface charge of red mud can be derived from pH measurements and determined by literature methods [83,84]. The point of zero charge (PZC) can be used in the determination of the surface charge properties of materials [83,84], and is defined as the pH at which the net charge on the surface is zero. The PZC provides an estimate of the acidity of the oxide surface. For most alumina and iron oxides the PZC is approximately 7–8 [85,86], with Fe_2O_3 and Al_2O_3 having PZC values of 8.5 and 9.2 respectively. The PZC of hematite is 8.5–8.8 determine by potentiometric titration [87], while goethite has a PZC of around 8.9–9.5 [38,88,89]. Some studies have shown that red mud has a PZC value of about 6.5 [3], while others have reported PZC values of around 8.3 [76,90,91]. Red muds containing high silica usually have PZC values of 6.3, which suggests that the presence of these compounds reduces the PZC value. The presence of different oxides in red mud, means that there are not only neutral surface complexes and SOH sites at PZC, but also both positively charged (such as $FeOH_2{}^+$ and $AlOH_2{}^+$) and negatively charged (such as TiO^- and SiO^-) surface complexes [90]. The shift in PZC to lower values is believed to be attributed to the formation of differently charged oxide surface sites, and the release of free hydroxide ions back into solution resulting in the increase in positive surface charge.

1.4. Removal of trace metals from solution

Red mud has a strong binding capacity for heavy metals [6,12,13,15]. Red mud has the ability to adsorb trace metals from solution onto the very fine grained iron oxides. These finely grained particles have high surface/volume and high charge/mass ratios when the pH of the solution is above 5 [92,93], which increases the ability of red mud to remove trace metals. Increased adsorption efficiency can also be achieved by ensuring the solution pH is greater than 5 [94,95]. High adsorption affinity of heavy metals on red mud is attributed to the chemisorption reactions at the surface of the oxide components of red mud (e.g. Fe_2O_3, Al_2O_3, TiO_2), however the identification of the oxide with the highest affinity for a given metal ion has not been determined [18,19,96]. The ability of red mud to remove trace metals from solution has been found to increase over time, where 1 kg of dry red mud was able to remove approximately 1000 meq./kg of trace metals from solution [96]. Adsorption of heavy metals from solution increases with increased contact of the solution with red mud, rendering heavy metal removal a time dependent process. The metal concentrations retained in red mud can be calculated using Eq. (18). Santona et al. [19], investigated red muds with high levels of cancrinite (zeolite-like structure), and suggested that higher adsorption values obtained were due to the presence of large quantities of cancrinite, which incorporated the heavy metal cations in the cages and channels of its structure.

$$q_e = \frac{(C_0 - C_e)V}{m} \tag{18}$$

where, q_e is the sorbent phase (mg/g), C_0 and C_e are the initial and final equilibrium concentrations of the metal ion in solution (mg/l), V is the solution volume (l) and m is the mass of the sorbent (g).

The mechanism for the removal of dissolved metals using red mud has been proposed to be comprised of four steps:

(i) co-precipitation of their insoluble metal hydroxides that form successive layers on the red mud surface,
(ii) formation of kinetic intermediates $[Fe_2(OH)_4]^{2+}$, $[Fe_3(OH)_4]^{5+}$, $[Al_4(OH)_8]^{2+}$, and $[Al_8(OH)_{20}]^{4+}$, at the adsorbent surface,
(iii) chemical adsorption which removes metal ions as uncharged hydroxides condensed onto surface hydroxyl groups exposed on the red mud surface [97] and
(iv) ion exchange.

The dominant mechanisms of removal are believed to be (i) and (iii) [98,99].

1.5. Acid neutralising capacity (ANC)

The abundance of amorphous and finely crystalline phases present in red mud gives rise to its high theoretical acid neutralising capacity of 3.6 mol/kg [11,96]. Neutralised red mud, pH 8.6, retains a high neutralising capacity due to the presence of large quantities of acid neutralising carbonate minerals and finely crystalline minerals that form weak bases. McConchie et al. [96], determined the neutralisation of red mud is initially rapid, and increases slowly when approaching its neutralisation limit of 3.65 mol of acid/kg after a 48 h period. No further

improvement was observed after 48 h. The ANC of seawater neutralised red mud can be calculated, using Eq. (19).

$$\text{Total OH-alkalinity} = [Na^+] + 2[Ca^{2+}] + 2[Mg^{2+}] \quad (19)$$

where [concentrations] are in mmol/g.

2. Seawater neutralised bauxite refinery residues

2.1. Introduction

Bauxite refinery residues are characterised by relatively high concentrations of sodium aluminate and sodium carbonate and a variety of anionic species. If left untreated, these species have the potential to be detrimental to the environment. Therefore, systems have been developed to remove these species prior to disposal. Several groups have explored seawater neutralisation of bauxite refinery residues [10,11,100,101]. A number of alumina refineries have implemented the neutralisation of the bauxite refinery residue with seawater prior to disposal, and found it provided a reduction in both pH and dissolved metal concentrations. Glenister and Thornber [10], concluded disposal of refinery residues at pH 8 was optimal, since at this pH chemically adsorbed Na is released, neutralising alkaline buffer minerals and rendering most of the dissolved metal species insoluble. This coincides with the recommended pH value outlined by environmental departments [9]. Seawater neutralisation results in the neutralisation of alkalinity through the precipitation of Mg, Ca, and Al hydroxide and carbonate minerals [102]. Some researchers have investigated the neutralisation of red mud with strong acids [77,98,102,103], and have found that the initial addition of acid results in a rapid decrease in pH, followed by the leaching of alkaline solids from the red mud causing a slow rise in pH.

Implementation of seawater neutralisation of red mud at Queensland Alumina Ltd. (QAL) initially began as an alternative to the use of freshwater [100], and led to the discovery of the many benefits, including:

(i) a decrease in freshwater use [100],
(ii) increased settling rates of ponds due to agglomerate consolidation [104],
(iii) decreased alkalinity and sodicity in the solid refinery residue and entrained liquor [100],
(iv) increased acid neutralisation capacity, and
(v) improved soil properties after rehabilitation.

2.2. Reaction mechanism

The addition of seawater to un-neutralised red mud results in the formation of fine mineral particles that flocculate into larger agglomerates. Multivalent exchange cations, Ca and Mg, form electrostatic bridges [105] which then act as nucleation sites for the precipitation of magnesium and calcium hydroxides. Hanahan et al. [11], reported an increase in electrical conductivity indicating the increase in soluble salt content. Formation of these hydroxides reduces the concentration of hydroxide ions in solution, therefore reducing the pH of the solution [106]. As the electrostatic conditions of the surface changes, the agglomerates tighten, pH decreases, and elements that exhibited colloidal behaviour initially at high pH lose stability [105]. The further decrease in pH causes the precipitation of hydroxycarbonates of aluminium, calcium, and magnesium, where the precipitation of hydrotalcite-like compounds, becomes favoured [11].

Seawater neutralisation does not eliminate hydroxide from the system but converts the readily soluble, strongly caustic refinery residue into less soluble, weakly alkaline solids. The carbonate and bicarbonate alkalinity of the waste is primarily removed through the precipitation of calcite and aragonite [106]. McConchie et al. [96], described the seawater neutralisation process as the precipitation of hydroxyl ions predominantly as brucite, but also as boehmite, gibbsite, hydrocalumite, hydrocalcite, and *p*-aluminohydrocalcite. Most of the boehmite, gibbsite, hydrocalumite, hydrotalcite, and *p*-aluminohydrocalcite was already present in red mud, however, the reduction in pH after seawater neutralisation influenced the continuation of crystal growth as aluminium became less soluble [96]. Menzies et al. [7], reported the formation of a white precipitate containing hydrotalcite, aragonite, and pyroaurite, determined by XRD. The extensive characterisation of seawater neutralised red mud by Hanahan et al. [11], revealed the complexity of the system, identifying 15 mineral components (XRD). The major elemental components of seawater neutralised red mud, determined by acid digestion and ICP-MS, were Fe > Na > Al > Ca > Si > Mg [11]. Variations in reported values and components of seawater neutralised red mud are due to the differences in physical, chemical, and mineralogical properties of red mud.

2.3. Formation of hydrotalcite

The seawater neutralisation of aluminate liquor studies done by Smith et al. [107,108], reported that the exact composition of the precipitate, including hydrotalcite, calcite and aragonite, is dependent on the precipitation conditions. Smith et al. [107,108], found that the composition of the hydrotalcite was dependent on the pH, where hydrotalcite formed at high pH (pH > 13) had a Mg:Al ratio of 2:1 (Eq. (20)), while those precipitated at pH 8 had a Mg:Al ratio of 4:1 (Eq. (21)). At high pH a more stable microcrystalline carbonate hydrotalcite ($Mg_4Al_2(CO_3)(OH)_{12}{\cdot}xH_2O$) forms, due to the readily adsorbed CO_2 from the atmosphere producing a saturated carbonate solution. At lower pH (pH <9.5) a less well defined crystal structure forms. Due to the decrease of available carbonate in solution, the intercalation of other anions into the hydrotalcite structure ($Mg_8Al_2Cl(CO_3)_{0.5}(OH)_{20}{\cdot}xH_2O$) is possible. The decrease in available carbonate is due to the rapid decrease in hydroxide ions from solution resulting in a lower adsorption of CO_2, and therefore a decrease in available carbonate anions for intercalation, Eq. (22).

$$4MgCl_2 + 2NaAl(OH)_4 + NaOH + Na_2CO_3 \rightarrow Mg_4Al_2(CO_3)(OH)_{12}{\cdot}xH_2O + 8NaCl \quad (20)$$

$$8MgCl_2 + 2NaAl(OH)_4 + 12NaOH + 1/2Na_2CO_3 \rightarrow Mg_8Al_2Cl(CO_3)_{0.5}(OH)_{20}{\cdot}xH_2O + 15NaCl \quad (21)$$

$$CO_2 + 2Na^{2+} + 2OH^- \rightarrow 2Na^{2+} + CO_3{}^{2-} + H_2O \quad (22)$$

Seawater neutralised red mud would consist of both the 2:1 and 4:1 hydrotalcite, where a small quantity of the 2:1 hydrotalcite would precipitate initially before the predominant 4:1 hydrotalcite forms at the reduced pH. The reduced level of carbonate in solution allows for the inclusion of other anions, such as oxy-anions of transition metals, vanadate and molybdate, into the hydrotalcite matrix. The rate of adsorption of anions other than carbonate depends on the concentration of carbonate in solution. Carbonate is the predominant anion that is intercalated into the hydrotalcite structure, therefore its presence hinders the intercalation of other anionic species. Increase in temperatures showed a slight increase in adsorption efficiency [107], suspected to be attributed to the decrease in carbonate through the conversion of carbonate to CO_2 at higher temperatures.

2.4. Adsorption of anions on the surface of neutralised red mud

Removal of contaminates is not only limited to the intercalation of species in hydrotalcite, but also through the adsorption of contaminants onto the surface of neutralised red mud. Genc et al. [5], investigated the adsorption of arsenate from water using neutralised red mud and found that adsorption of arsenate increased with decreased pH (agrees with the work by Smith et al. [107,108]), higher adsorbent concentrations and lower initial arsenate concentrations. Seawater neutralised red mud consists of a complex mixture of fine grained iron and aluminium hydroxides and hydrocarbonates that exhibit a pH dependent surface charge [5,91] and it was suggested that the pH dependence of arsenate adsorption onto seawater neutralised red mud was through the exchange of an aqueous ligand for a surface hydroxyl group, Eq. (23). The number of positively charged surface sites available for adsorption is higher at pH 6.3, and decreases with increased pH [5,91]. Adsorption is believed to be facilitated by the electrostatic and chemical attraction of arsenate for the positive surface charge [5,91]. Adsorption increases when the pH of the solution is lower then the PZC of red mud, due to the increase of positive charge on the red mud surface. At high pH values, anions may be competing with hydroxide ions, for the minimal number of positively charged sites on the red mud surface, which causes the decrease in adsorption.

$$\equiv S{-}OH + L^- + H^+ \leftrightarrow \equiv S{-}L + H_2O \quad (23)$$

where, ≡S represents the seawater neutralised red mud surface.

The Langmuir isotherm, Eq. (24), is a commonly used adsorption isotherm for assessing the potential uses of an adsorbent for particular applications. The Langmuir isotherm has been used to study the adsorption capacity of seawater neutralised red mud [18,19]. To determine whether anion adsorption by seawater neutralised red mud is a high-affinity adsorption, the dimensionless constant separation term R_L can be calculated, Eq. (25).

$$q_e = \frac{(Q_0 b C_e)}{(1 + bC_e)} \quad (24)$$

where, b is the adsorption constant related to the enthalpy of adsorption ($1\,\mu mol^{-1}$), Q_0 is the adsorption capacity ($\mu mol\,g^{-1}$), and C_e is the equilibrium concentration (μM).

$$R_L = \frac{1}{(1 + bC_0)} \quad (25)$$

where, C_0 is the initial anion concentration (μM) [26,109].

The parameter R_L indicates the shape of the adsorption isotherm and $0 < R_L < 1$ corresponds to high affinity adsorption [5]. Arsenate adsorption by seawater neutralised red mud was found to be very efficient regardless of the pH or the initial concentration [5]. Unseren et al. [98], and Altundogan et al. [110], have reported adsorption follows the chemisorption mechanism for heavy metal cations.

3. Layered double hydroxides (LDH)

3.1. Introduction

Layered double hydroxides (LDHs) have been extensively researched for many years as host materials for a range of anionic exchange reactions, proving to be beneficial in the removal of anionic impurities in solutions [111–123]. They are sometimes referred to as anionic or hydrotalcite-like clays, and are based on the brucite structure, $Mg(OH)_2$ [124–126]. LDHs are represented by the general formula $[M_{1-x}{}^{2+}\,M_x{}^{3+}(OH)_2]^{x+}A_{x/m}{}^{m-}{\cdot}nH_2O$, where M^{2+} is a divalent cation, M^{3+} is a trivalent cation and A an interlamellar anion with charge m^-. Pure LDH phases exist for $0.2 \leq x \leq 0.33$. Values outside the specified x range will form: (i) boehmite (α-AlOOH) for $x > 0.337$, (ii) hydromagnesite ($4MgCO_3{\cdot}Mg(OH)_2{\cdot}4H_2O$) for $0.105 < x < 0.201$, and (iii) a mixture of hydromagnesite and $Mg(OH)_2$ for $x < 0.105$ [127–130]. Hydrotalcite is produced when $M^{2+} = Mg^{2+}$ and $M^{3+} = Al^{3+}$, giving the general formula $Mg_6Al_2(OH)_{16}CO_3{\cdot}4H_2O$.

LDHs consist of layers of metal cations (M^{2+} and M^{3+}) of similar radii, which are randomly distributed in the octahedral positions, that form brucite-like structures $M(OH)_2$, Fig. 7. The

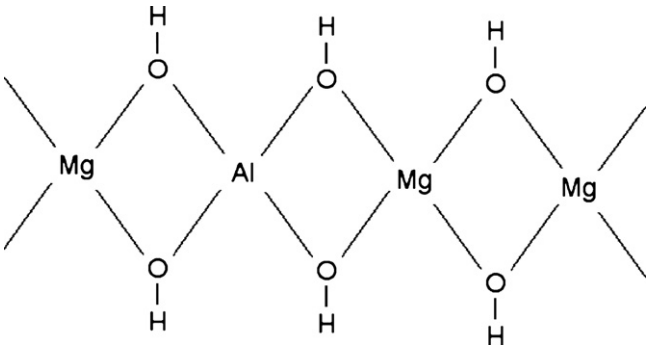

Fig. 7. Schematic representation of the hydroxide layers in the hydrotalcite.

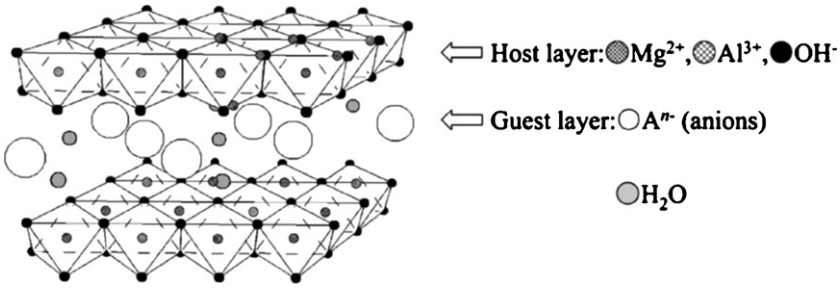

Fig. 8. Schematic representation of the hydrotalcite structure.

enthalpy of bond formation within the layers is largely responsible for the thermodynamic stability of these layered materials [131]. The brucite-type layers are stacked on top of each other and are held together by weak interactions through the hydrogen atoms [132]. Substitution of divalent cations for trivalent ones gives rise to positively charged layers, where a maximum of one in three trivalent sites are substituted by a divalent cation [128]. The ratio of M^{2+} to M^{3+} cations determines the degree to which the framework is positively charged, where a low M^{2+}:M^{3+} ratio will result in highly positively charged layers. To maintain electroneutrality, the interlamellar domain must be occupied by an adequate number of anions, which are generally hydrated (Fig. 8) [127,133,134]. Charge neutrality is not confined to the interlayer region, but also to the external surfaces of the LDH structure. The resulting mineral has layers of ordered cations between hydroxyl sheets, giving hydrotalcites the acronym LDHs or 'double layer hydroxides'. As there is no overall charge, hydrotalcites are quite stable.

The interlayer region of LDHs is complex, consisting of anions, water molecules, and other neutral or charged moieties. A large variety of anionic species can be positioned between the hydroxide layers, including halides, oxy-anions, oxy and polyoxy-metallates, anionic complexes, and organic anions [135]. The interlayer interactions of LDHs are mediated by coulombic forces between the positively charged layers and the anions in the interlayer, and hydrogen bonding between the hydroxyl groups of the layer with the anions and the water molecules in the interlayer [135,136]. Water molecules are connected through extensive hydrogen bonding to the hydroxyl ions of the metal hydroxide layers and interlayer anions [134,137,138]. The quantity of water present in the interlayer is governed by the nature of the interlayer anions, water vapour pressure, and temperature [139–143]. Khan and O'Hare found, using NMR techniques, that water molecules are in a continuous state of flux [127]. However, vibrational studies have shown that the hydrotalcite interlayer has a highly structured yet mobile environment [144–146] (Fig. 8).

Many types of hydrotalcites can be formed from different combinations of divalent and trivalent cations and different interlayer anions. Some natural LDHs are given in Table 3. The orientation of the ions in the interlayer is determined by factors such as the charge of layers and the amount of interlayer water present. The anion may be divalent (carbonate or sulphate), or it may be monovalent (hydroxide, chloride, or nitrate) [147–153]. An increase in anionic charge results in the electrostatic interactions between the positively charged hydroxide layer and the anion to become stronger, therefore rendering a more stable hydrotalcite. This means the formation of a hydrotalcite with a divalent anion is more favourable over one containing monovalent anions [154–156].

3.2. Preparation of LDHs

A variety of methods exist for LDH production such as co-precipitation [157–159], urea reduction [160,161], salt-oxide method [162], hydrothermal [158,162], electrochemical

Table 3
Compositions, crystallographic parameters and symmetries for some natural LDHs

Name	Chemical composition	Unit cell parameters		Symmetry
		a (nm)	*c* (nm)	
Hydrotalcite	$Mg_6Al_2(OH)_{16}CO_3{\cdot}4H_2O$	0.3054	2.281	3R
Manasseite	$Mg_6Al_2(OH)_{16}CO_3{\cdot}4H_2O$	0.3100	1.560	2H
Meixnerite	$Mg_6Al_2(OH)_{16}(OH)_2{\cdot}4H_2O$	0.3046	2.292	3R
Pyroaurite	$Mg_6Fe_2(OH)_{16}CO_3{\cdot}4.5H_2O$	0.3109	2.341	3R
Sjögrenite	$Mg_6Fe_2(OH)_{16}CO_3{\cdot}4.5H_2O$	0.3113	1.561	2H
Caolingite	$Mg_{10}Fe_2(OH)_{24}CO_3{\cdot}2H_2O$	0.3120	3.750	3R
Iowaite	$Mg_{4.63}Fe_{1.32}(OH)_{16}Cl_{1.22}{\cdot}1.95H_2O$	0.3119	2.425	3R
Stichtite	$Mg_6Cr_2(OH)_{16}CO_3{\cdot}4H_2O$	0.3100	2.340	3R
Barbertonite	$Mg_6Cr_2(OH)_{16}CO_3{\cdot}4H_2O$	0.3100	1.560	2H
Desautelsite	$Mg_6Mn_2(OH)_{16}CO_3{\cdot}4H_2O$	0.3114	2.339	3R
Takovite	$Ni_6Al_2(OH)_{16}CO_3{\cdot}4H_2O$	0.3025	2.259	3R
Reevesite	$Ni_6Fe_2(OH)_{16}CO_3{\cdot}4H_2O$	0.3081	2.305	3R

Where, 3R represents a rhombohedral stacking, while 2H represents a hexagonal stacking sequence.

[163,164], and sol–gel [126]. The most frequently used methods are co-precipitation and urea reduction, while electrochemical and sol–gel are the least used methods. Co-precipitation is based on the slow addition of a mixed solution of divalent and trivalent metal salts to an alkaline solution in a reactor, which leads to the co-precipitation of the two metallic salts. Formation of the LDH is based on the condensation of hexa–aqua complexes in solution that form the brucite-like layers containing both metallic cations [135]. Interlamellar anions either arise from the counter-anions of the metallic salts, or anions from the alkaline solution. At high pH, hydroxyl ions are prevalent and therefore can be intercalated, however if the alkaline solution is prepared with sodium carbonate the intercalated anion is carbonate due to its higher affinity for the LDH interlamellar region [165].

In order to obtain well organised phases, the preparation conditions have to be optimised for the desired product. For well ordered hydrotalcite-like structures to form, a pH range between 7 and 10 is required. At lower pH values, an amorphous compound is obtained, while at higher pH values $Mg(OH)_2$ crystallises with the LDH phase [135]. The study conducted by Crepaldi et al. [133], on the comparison of constant and variable pH co-precipitation reactions demonstrated that maintaining a constant pH throughout the reaction yielded LDHs with higher crystallinity, smaller average particle sizes, higher average specific surface area, and higher average pore diameters, in comparison to those produced with variable pH. Scanning electron microscopy showed that variable pH also leads to heterogeneous products, due to the different precipitates produced initially at high pH, while those obtained at lower pH showed particles homogeneously aggregated [133].

3.3. Anionic exchange

Recent studies have focused on using LDHs ability to undergo anionic exchange reactions in a wide range of applications, especially in the removal of toxic anions from aqueous systems [111,166–169]. The interlayer region is less stable then the brucite-like layers, and therefore readily undergoes anion exchange reactions. The interlayer interactions can be direct [170] or mediated through other species present in the interlayer region [171]. LDHs predominantly have mediated interlayer interactions, making the mechanism for anion exchange complicated. Controversy exists in the literature regarding exact mechanism of anion exchange reactions involving LDHs [127,156,172,173]. The general assumption is a topotactically mechanism [154,155], however other mechanisms have been proposed including: (i) a two-step process involving the dissolution of the LDH phase followed by the re-precipitation of the new LDH with the desired anion (D-R mechanism) [174], (ii) first order kinetics [175], or (iii) another two-step mechanism involving the adsorption of the incoming anion followed by the desorption of the initial anion in the interlayer [176,177].

Anion exchange reactions are thought to take place topotactically based on the assumption that a close structural relationship between parent and product phases exist. The only structural change brought about by anion exchange is a variation in the interlayer distance, which is dependent on the size of the incoming anion. However, observations have been noted in recent studies that suggest the anion exchange reaction follows the D–R mechanism. The observations included a mass loss of the LDH during anion exchange reactions, which can be attributed to bulk dissolution [178–180], and unitary salts formed as impurity phases during anion exchange reactions [181].

According to the topotaxy mechanism [182], the lamellar structure of LDHs allows for the anion diffusion of anionic species in the interlayer regions for anions of higher affinity, shown in Eq. (26).

$$[M^{II}–M^{III}–\mathbf{X}] + \mathbf{Y} \rightarrow [M^{II}–M^{III}–\mathbf{Y}] + \mathbf{X} \quad (26)$$

Where, $M^{II}–M^{III}$ are the positively charged hydroxide layers; X represents the anionic species in the interlayer; Y represents an anionic species with a higher affinity for the interlayer region which will replace X.

According to Eq. (26), the outgoing **X** anion is exchanged for the incoming **Y** anion in a single step, where the host hydroxide layer essentially remains unperturbed. A two-step topochemical reaction has also been proposed [176], where the initial step is the separation of the LDH lattice into its corresponding positively charged hydroxide layers and free anions, Eq. (27), followed by the restacking of the highly reactive layers to form the LDH with the new anionic species incorporated into the interlayer region, Eq. (28).

$$[M^{II}–M^{III}–\mathbf{X}] \rightarrow [M^{II}–M^{III}]^{+} + \mathbf{X} \quad (27)$$

$$[M^{II}–M^{III}]^{+} + \mathbf{Y} \rightarrow [M^{II}–M^{III}–\mathbf{Y}] \quad (28)$$

It was surmised that under certain conditions of temperature, pH, and anion concentration, that the precursor LDH could dissolve (dissolution step, Eq. (29)), where the dissolved cations would re-precipitate with the incoming anions (re-precipitation step, Eq. (30)). Intercalation of the new anionic species is based on two factors; (i) it has a higher affinity than the original anionic species, and (ii) the formation of the new LDH has a greater thermodynamic stability than the original LDH structure, reflected by a lower solubility product [131]. Radha et al. [131], proposed the D–R mechanism, based on the fact that no reliable estimates of the strengths of these interactions and how they compare with the strength of interlayer bonding has been reported in literature.

$$[Mg_2Al(OH)_6]NO_3\cdot 2H_2O \rightarrow 2Mg^{2+} + Al^{3+} + 6OH^{-} + NO_3{}^{-} + 2H_2O \quad (29)$$

$$2Mg^{2+} + Al^{3+} + 6OH^{-} + 1/nX^{n-} + 2H_2O \rightarrow [Mg_2Al(OH)_6](X^{n-})_{1/n}\cdot 2H_2O \quad (30)$$

Identifying which mechanism is responsible for anion exchange reactions has proven to be difficult due to: (i) the high rate of anion exchange reactions, making kinetic studies difficult, (ii) intermediate phases formed are highly unstable and react quickly to form the new LDH phase, and (iii) in the D–R mech-

anism, the dissolution of LDH takes place at the solid–liquid interface [131].

Extensive studies by Miyata et al. [130,138,183], exposed the anionic exchange properties of a number of species, establishing a ranking of affinity for intercalation. Hydrotalcite shows the greatest affinity for anions of high charge density [183,184]. The affinity of monovalent anions was determined to be $OH^- > F^- > Cl^- > Br^- > NO_3^- > I^-$, while the order for divalent anions was $CO_3^{2-} > SO_4^{2-}$. The carbonate anion has proven to be the preferred anion for intercalation, and once intercalated proves very difficult to exchange with other anions. The high affinity of carbonate in Mg, Al hydrotalcites prevents its use as an anion-exchange material, unless precautionary steps (nitrogen atmosphere and carbonate free solutions) or calcination are used to minimise the carbonate content in the hydrotalcite matrix.

Theoretically, LDHs have an anion exchange capacity of 3.6 meq./g if all the carbonate in the general formula was exchanged [183]. Experiments conducted by Miyata et al. [183], showed that a hydrotalcite prepared under a nitrogen atmosphere with carbonate free solutions could obtain an anion exchange capacity of 3 meq./g. The theoretical capacity value cannot be obtained due to hydroxide anions present in solution competing with the desired anion [185]. Removal of carbonate from all sources is essential in exchange reactions, as any carbonate present in the exchange solutions will be incorporated preferentially to other anions. Anion exchange capacity values were determined by comparing the anion concentrations of the initial and final solutions after the addition of a known amount of hydrotalcite by atomic adsorption spectroscopy and the Dionex method [185].

3.4. Reformation of hydrotalcites

Recent studies have shown that LDHs can have a so-called 'memory effect' whereby a hydrotalcite material can be thermally treated to remove water, hydroxyl, and carbonate units from its matrix, then re-hydrated in an aqueous solution to return to its original structure [161,186]. The restoration of the layered structure in hydrotalcites is a 'structural memory effect' [187–189]. This so-called memory or restoration effect can be used effectively to remove harmful anions, both organic [120,123] and inorganic [159,161,190,191], from wastewater solutions.

The calcination of hydrotalcite, from temperatures of 350–800 °C, removes interlayer water, interlayer anions (carbonate anions), and hydroxyls. The result is the formation of periclase-like Mg, Al oxides. XRD studies have shown the collapse of the crystalline hydrotalcite to an amorphous magnesium oxide with dispersed aluminium ions as a solid solution [159,161,185,191]. The carbonate anions are decomposed to carbon dioxide (CO_2) and O^{2-}, leaving O^{2-} anions between the layers [130,183,192,193]. Re-hydrating the calcined product regenerates the LDH, where water is absorbed to reform the hydroxyl layers, as well as being absorbed into the interlayer along with the anion in solution [123].

Anions that are reabsorbed do not necessarily need to be the original anions, since any available anion in the re-hydrating solution will be absorbed. For example, the re-hydration of calcined hydrotalcites in carbonate free solutions will yield a carbonate free hydrotalcite. Parker et al. [185], reported a 50% decrease in adsorption in the anion exchange capacity of LDHs due to a slight alteration in the re-formed hydrotalcite. Heating to temperatures above 900 °C produces spinel ($MgAl_2O_4$), totally degrading the hydrotalcite lattice and preventing any reformation.

3.5. Characterisation of LDHs

3.5.1. Vibrational spectroscopy – infrared (IR) and Raman spectroscopy

Spectroscopy has been a widely used technique in the industry for the structural and compositional analysis of inorganic, organic, organometallic, metal organic, and polymeric materials. Vibrational spectroscopy involves the use of light to probe the vibrational behaviour of molecular systems, usually via absorption, emission, or light scattering experiments. Both infrared and Raman spectroscopy give rise to a vibrational spectrum as a set of absorption or scattering peaks, corresponding to the energies of transitions within the sample (frequencies of vibrational modes).

3.5.1.1. Hydroxyl stretching and bending vibrations. The vibrational spectra of hydrotalcites exhibit various forms of water hydroxyl-stretching vibrations. These include water in the interlayer between the hydroxide layers, which may or may not form bridging-type bonds with the exchangeable anions, water adsorbed on the outer surface, and free water between layers. Water hydroxyl-stretching vibrations are intense in an infrared spectrum, because of the large change in dipole moment, whereas, water is not always observed in the Raman spectrum. Therefore, the comparison of the two techniques allows for the identification of the bands associated with water and those associated with hydroxyl stretching vibrations. Water bending modes are situated around 1600–1700 cm^{-1} accompanied by OH-stretching vibrations in the 3000–4000 cm^{-1} region [160,194–196].

The replacement of Mg^{2+} by Al^{3+}, in hydrotalcites, results in stronger hydrogen bonds between the hydroxide layers, when compared with brucite, due to Al^{3+} having a higher charge and smaller ionic radius [197]. This change in O–H bond lengths can be detected in infrared spectra with shifts to higher frequencies in the bending region, and shifts to lower frequencies in the stretching region associated with the strength of the hydrogen bonds [198]. A similar observation can be seen for the lattice translation modes in the low frequency region of the infrared spectra [199]. The OH-stretching vibration for brucite is situated around 3570–3555 cm^{-1}, while for Mg, Al hydrotalcites the corresponding band is located at around 3450 cm^{-1}. This shift is associated with the shorter O–H bonds existing in hydrotalcite than in brucite, causing an increase in the electrostatic attraction within the hydrotalcite layer [199].

Table 4
Frequencies (cm^{-1}) and assignments of the hydroxide layer modes of the types M—OH and M—O in the infrared spectra of Mg/Al-layered double hydroxides in comparison to brucite $Mg(OH)_2$

Brucite	Reference source								Assignment
	[204]	[139]	[205]	[206]	[207]	[208]	[199]	[209]	
–	CO_3	CO_3	CO_3	NO_3, SO_4, Cl	CO_3	CO_3	CO_3, NO_3, OH	CO_3	Interlayer anion present
3570								3597	$A_{2u}\nu_1$(OH—HOH) or "Mg/Al"—OH
	3480	3470	3421	3392–3422	3441	2700–4000	3440–3478	3467	$A_{2u}\nu_2$(OH—HOH) or "Al"—OH
			998	985	950	960–945		939	ν_{sym} anion or ν_{def} Al—OH
		865	799	853–830	874	850	857–856	870	E_u(OH) or $\nu_2CO_3^{2-}$
680		670	651	668	671	663	686–663	635	E_u(OH) or "Mg"-(OH) translation
455		na	na	616–584	556	555	553–550	553	$A_{2u(T)}$ or "Al"—OH translation
365		na	na	426–419	451	451	448–440		$E_{u(T)}$

Extensive overlapping of bands exists in the OH-stretching region of LDHs between metal–OH bands of the hydroxide layers and the OH-bands of water. For water adsorbed on clay minerals, the OH-stretching modes of weak hydrogen bonds occur in the region between 3580 and 3500 cm^{-1}, while strong hydrogen bonds are observed below 3420 cm^{-1}. Water co-ordinated to cations shows stretching vibrations occurring around 3220 cm^{-1} [198]. Fourier Transform IR spectra obtained by Jose dos Reis et al. [200], showed a broad band at 3400 cm^{-1} assigned to the ν(OH) mode ascribed to interlayer water and hydroxyl groups in the hydroxide layers of hydrotalcite. Numerous studies conducted by Kloprogge and Frost (summarised in Table 4) have reported the infrared hydroxyl modes of Mg, Al hydrotalcites [198]. A broad band around 3300–3000 cm^{-1} with a shoulder, sometimes visible, comprised of two or three overlapping bands are attributed to the OH-stretching vibrations and a stretching vibration of interlayer water. The shoulder at 3050 cm^{-1} was assigned to hydroxyl interactions with carbonate ions in the interlayer [138,198,200–203], and has been attributed to the bridging mode H_2O–CO_3^{2-}.

The corresponding H–O–H bending vibration of interlayer water interacting with interlayer carbonate is located at around 1750 cm^{-1} [210]. The high vibrational frequency is attributed to symmetry restrictions induced by the hydrogen bonded carbonate ions to hydroxyl groups of the hydroxide sheets [201,210]. Fig. 9 shows where water and hydroxyl group vibrational frequencies originate from within the hydrotalcite structure of Ni, Al and Co, Al calcined hydrotalcite samples. Slight shifts in these values are expected for Mg, Al hydrotalcite structures.

A weak peak around 1630 cm^{-1} in the infrared spectrum is attributed to the δH_2O mode of interlayer water [194–196,198,200,211,212], while the OH-bending vibrations are located at around 1040 cm^{-1} in the Raman spectrum. The interlayer anion has been found to have an effect on the position of the OH-bending mode of interlayer water, shown in Table 5.

The OH-stretching vibrational modes are weaker but sharper in the Raman spectrum compared to the corresponding modes in the infrared spectrum. Raman bands observed around 3600–3450 cm^{-1} are attributed to the stretching frequencies of hydroxyl groups bonded to Al, Mg or a combination of both. Table 6 illustrates some reported literature values and the corresponding assignments. Two bands around 470 and 550 cm^{-1}

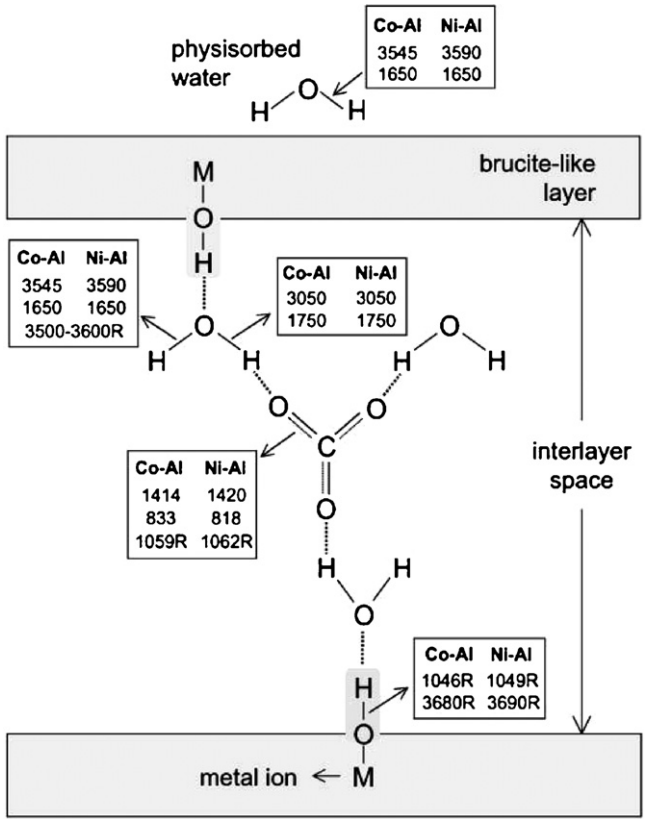

Fig. 9. Water, hydroxyl and carbonate vibrations in the interlayer of Co and Ni hydrotalcites [201].

Table 5
Infrared water bending vibrational positions of Mg, Al hydrotalcites as a function of the interlayer anion, as reported in literature [135]

Interlayer anion	Band position (cm^{-1})
CO_3^{2-}	1640
CO_3^{2-}	1655
CO_3^{2-}	1591
CO_3^{2-}	1647
OH^-	1628
OH^-	1625
NO_3^-	1629
SO_4^{2-}	1642
CrO_4^{2-}	1639
$V_{10}O_{28}^{6-}$	1653

Table 6
Frequencies (cm^{-1}) and assignments of the hydroxide layer modes of the type M—OH and M—OH in the Raman spectrum of Mg/Al-layered double hydroxides

[197]	[199]	[209]	Assignment
3560	3572	3580	A_{1g}(OH) or "Mg/Al"—OH
3460	3454	3454	A_{1g}(OH—HOH) or "Al"—OH
		3358	
	1061	1053	$E_{g(R)}$(OH)
		979	
	695	694	$E_{g(R)}$ or $\nu_4(E')CO_3$
	557	552	$E_{u(T)}$
	483	476	$A_{1g(T)}$
	393	388	$A_{1g(T)}$
	307	303	Acoustic overtone

have been assigned as hydroxyl groups associated with Al or Mg [201,209]. The band at 470 cm^{-1} is only Raman active, while the band at 550 cm^{-1} has an equivalent mode in the infrared spectrum in the same location.

3.5.1.2. Carbonate stretching vibrations. When the carbonate species is present as a free ion, it will exhibit a planar triangle with point symmetry D_{3h}. Group theoretical analysis of the carbonate ion predicts four normal modes: the ν_1 symmetric stretch of A_1 symmetry normally observed at 1063 cm^{-1}, the antisymmetric stretch of E' symmetry observed at 1415 cm^{-1}, the ν_2 out of plane bend at 879 cm^{-1} and the in-plane bend at 680 cm^{-1} [213,214]. All modes are both Raman and infrared active except for the ν_2 mode, which is IR active only. Incorporation of the carbonate species into the hydrotalcite structure will exhibit a shift towards lower wavenumbers, due to the interaction of carbonate with interlayer water molecules and/or hydroxyl groups from the hydrotalcite layer.

Hydrotalcites with carbonate incorporated into the interlayer typically show infrared bands at around 1360–1400, 875 and 670 cm^{-1}. Assignments for the carbonate modes are outlined in Table 7. A strong peak at around 1360 cm^{-1} observed by Jose dos Reis et al. [200], attributed to the ν_3 mode of the carbonate species, agreed with literature values. An additional band at 1550–1500 cm^{-1} has been reported [215,216], and attributed to the formation of a bicarbonate ion upon dehydration (proton transfer from the hydroxide sheets to the carbonate ion). The presence of this band indicates a change in the carbonate symmetry. In the Raman spectrum the symmetrical stretching vibration $\nu_1(A'_1)$, the antisymmetric stretching vibration $\nu_3(E')$, and the bending angular vibration $\nu_4(E')$ around 1063, 1415,

Table 7
FT-IR interlayer carbonate vibrational modes [207,209]

Mode	Mg, Al hydrotalcite (cm^{-1}) [209]	Mg, Al hydrotalcite (cm^{-1}) [207]
$\Delta\nu_3$	36	36
ν_{3a}	1401	1400
ν_3	1365	1364
ν_1	1012	1060
ν_2	870	874
ν_4	667	671

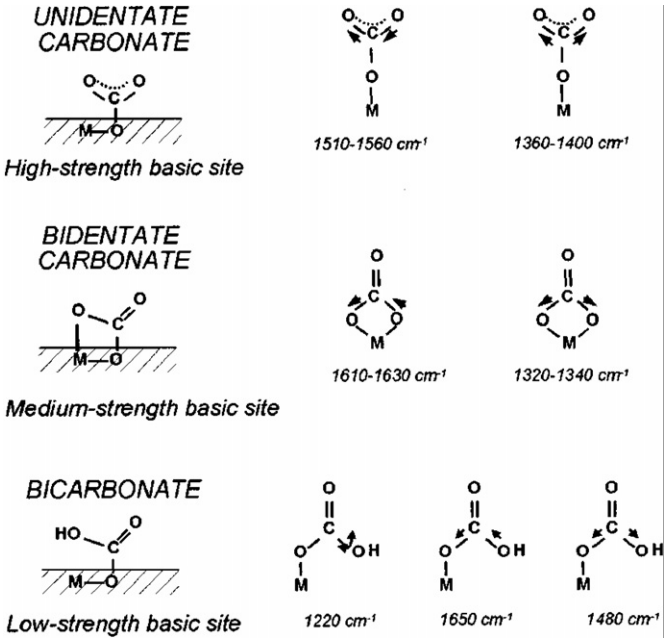

Fig. 10. Infrared bands of adsorbed CO_2 surface species on calcined hydrotalcite [219,220].

and 680 cm^{-1}, respectively, are observed for the free carbonate anion [197,213,214]. Weak ν_3 and ν_4 band modes have been observed at around 1053 and 1403 cm^{-1} [197,209,217].

Exposure of hydrotalcite leads to the adsorption of CO_2 onto the hydrotalcite structure and has been characterised by infrared spectroscopy [201,218–220]. These studies reported the three different carbonate species: (i) unidentate carbonate, (ii) bidentate carbonate, and (iii) bicarbonate, shown in Fig. 10. These different carbonate species reflect different types of surface basic sites and their relative strengths. Unidentate carbonates were proposed to be bonded to high-strength basic sites, bidentate carbonate to medium-strength basic sites, and bicarbonate to low-strength basic sites [219,220]. The same relationship was seen in the study by Di Cosimo et al. [218]. Morterra et al. [219], and Philipp et al. [220], reported that the strength of the surface basic sites depends on the Al content of the adsorbing species, where an increase in Al content increases the basic site density. The increase in site density was attributed to the rearrangement of the MgO lattice by Al^{3+} cations, forcing adjacent oxygen anions to become co-ordinately unsaturated.

Di Cosimo et al. [218], reported unidentate carbonate exhibited a symmetric O–C–O stretching vibration at 1360–1400 cm^{-1} and an asymmetric O–C–O stretching vibration at 1510–1560 cm^{-1}, while bidentate carbonate showed a symmetric O–C–O stretching vibration at 1320–1340 cm^{-1} and an asymmetric O–C–O stretching vibration at 1610–1630 cm^{-1}. The bicarbonate species involves surface hydroxyl groups and showed a C–OH bending mode at 1220 cm^{-1} as well as symmetric and asymmetric O–C–O stretching modes at 1480 and 1650 cm^{-1}, respectively. Vibrational frequencies reported by Pérez-Ramírez et al. [201], for Ni, Al, and Co, Al calcined hydro-

talcites were shifted to lower wavenumbers then those reported by Di Cosimo et al. [218].

3.5.1.3. Lattice translational modes. The lower wavenumber region of the infrared spectrum, 1000–400 cm^{-1}, are complicated due to the presence of lattice translational modes (650 cm^{-1}), librational modes of hydroxyl and water molecules (1000–700 cm^{-1}), Al–O bonds (450 cm^{-1}) [208], and the $\nu_4(E')$ carbonate band (680 cm^{-1}) [197]. A broad complex band is also observed at around 650–600 cm^{-1} with [199,207–209,217] or without [205,206] a separate band at 550 cm^{-1} due to Al–O and Mg–O bonds. Interpretation of a band at 870 cm^{-1} appears to have some disagreement between authors, with some ascribing the band to the $\nu_2(A''_2)$ mode of the interlayer carbonate [197,209,217], while Kagunya [199], ascribed the band to the $E_{u(R)}$(OH) mode for LDHs with not only carbonate, but also with nitrate and hydroxyls as the interlayer anions. Both assignments are plausible due to the broadness of the band, indicating that a possible overlap of both bands may exist.

3.5.2. TGA/DTG/DTA

The decomposition of the Mg, Al hydrotalcite structure occurs in three steps:

(i) removal of adsorbed water (<100 °C),
(ii) elimination of the interlayer structural water (100–200 °C), and
(iii) the simultaneous dehydroxylation and decarbonation of the hydrotalcite framework (300–400 °C) [130,133,153,201,218,221–224].

A fourth decomposition step may occur for the loss of either a volatile anion species (e.g. Cl^-, NO_3^-, and CO_3^{2-}) or a non-volatile species in which the anion is included in the formation of a mixed metal oxide [133,223,224]. The determination of the decomposition steps of hydrotalcite depends on the dryness of the sample, stability of the interlamellar species, and possible guest–host interactions mobilising the hydroxyl groups in the hydrotalcite lattice [223]. The thermal decomposition of carbonate hydrotalcites consists of two decomposition steps between 300 and 400 °C, attributed to the simultaneous dehydroxylation and decarbonation of the hydrotalcite lattice. Water loss ascribed to dehydroxylation occurs in two decomposition steps, where the first step is due to the partial dehydroxylation of the lattice, while the second step is due to the loss of water interacting with the interlayer anions. Dehydroxylation results in the collapse of the hydrotalcite structure to that of its corresponding metal oxides, including MgO, Al_2O_3, and $MgAl_2O_4$ (at temperatures over 900 °C) [153,221]. The exact decomposition product relies on the hydrotalcite and its counter balancing anions.

The rate of dehydroxylation has been used as a measure of the thermal stability of the hydrotalcite structure, where a delay in dehydroxylation indicates a more thermally stable hydrotalcite [222–224]. Hydrotalcite stability is anion dependent [223], suggesting that hydrotalcite stability can be controlled by the incorporation of more stable, less reactive anions. The presence of oxy-anions has proven to be beneficial in the stability of the hydrotalcite structure, shown by the delay in dehydroxylation of hydrotalcites containing oxy-anions compared to carbonate hydrotalcites [223]. This is due to the substantial number of hydroxyl groups interacting with an extensive network of solvated hydrogen bonded anions. The asymmetric shape of the DTG curve obtained by Malherbe et al. [223], for oxy-anions indicated the presence of two types of interlamellar water, (i) free water molecules, and (ii) water molecules interacting with anionic species via hydrogen bonding. Existence of different interlamellar water has been reported by others and was suggested to be related to the charge density of the hydroxylated brucite-like sheets [225,226].

3.5.3. X-ray diffraction (XRD)

X-ray diffraction techniques are traditionally used for the characterisation of minerals [227–229]. Identification of minerals by this technique is based on the reflection of X-rays by the characteristic atomic lattice planes within the mineral crystal [230]. The X-ray diffraction pattern is a measurement of the distance between single planes of atoms in a crystal, providing a direct measure of the height of layers as well as information about the bulk properties of the sample, such as the crystalline phases present [230,231]. Since different crystalline materials have different cell parameters, space groups, and symmetry, characteristic diffraction patterns are produced.

X-ray diffraction can be used to distinguish between the two different stacking sequences of the brucite-type sheets in LDHs, rhombohedral (3R) and hexagonal (2H) [207,232].

Table 3 gives the symmetry and cell parameters for a few different natural LDH structures. Hydrotalcite normally crystallises with the rhombohedral 3R stacking sequence, which is the three layer form, the parameters of the unit cell being a and $c = 3c'$, where c' is the thickness of one layer (sheet + interlayer) [232]. The other stacking sequence, hexagonal (2H), usually forms manasseite [132], which is the two-layer form and is generally obtained at high temperatures [233]. A third stacking sequence, (1H), has been reported for the most hydrated variety of hydrotalcite compounds containing sulphate anions, however the symmetry of this structure is unknown [157].

Properties of anionic species, such as size, charge, orientation, and the interactions of the anionic species with the positively charged interlayer, contribute to the degree of intercalation and the separation between layers [127,135]. Anion exchange reactions can be monitored by the shifts of the basal reflections 003 and 006 [131]. The typical $d(0\,0\,3)$ spacing obtained for hydrotalcites is 7.9 Å [209,212,234]. Deviations in value of the $d(0\,0\,3)$ basal spacing are associated with the type of anionic species intercalated into the interlayer region. Smaller basal spacings are generally associated with ions with small ionic radii. Inorganic species are typically smaller than organic species and as a result have smaller basal spacings values. Miyata and Kumura [235], showed that the separation of the layers, determined by the $(0\,0\,6)$ d-spacing, increased linearly with an increasing number of carbon atoms of the anionic species. Kooli et al. [236], reported a high layer charge, associated with low Mg:Al ratios, resulting in greater electrostatic

repulsions between the positively charged layers, and larger basal spacings.

3.6. LDHs in the alumina industries

LDHs have the potential to be used for the removal of a variety of organic and inorganic species in the Bayer process. The removal mechanism has been postulated to be a combination of intercalation and adsorption of the anionic species on the external surfaces, where small anions are intercalated while larger organic molecules are adsorbed [237–241]. Hydrotalcite and hydrocalumite ($Ca_2Al(OH)_6(Cl_{1-x}(OH)_x)\cdot 3H_2O$) are two types of LDHs that have been studied for the application of impurity removal in Bayer liquors.

Hydrotalcite has been researched for its use as a method to remove the organic impurity humate present in Bayer liquor. Schepers et al. [241], proposed the addition of magnesium compounds to contaminated Bayer liquors, and found a brown precipitate formed containing magnesium and aluminium hydroxides. The brown precipitate was thought to be an impure hydrotalcite formed from the in situ reaction of the magnesium salt and aluminate anion. Misra [237,238], reported that impure hydrotalcite formed from combining magnesia [$Mg(OH)_2$] with Bayer liquor, while high purity hydrotalcite could be formed from calcined (500–900 °C) magnesia. The reduction of humate concentration in the Bayer liquor was suggested to be due to surface adsorption rather than intercalation of the anion. This assumption was based on the large size of the humate molecules which would not physically fit between the hydrotalcite layers. The Queensland Alumina Ltd. (QAL) refinery also used hydrotalcite to investigate the extent of humate removal, and found that the quantity of humate substances decreased. Again it was suggested that the positive charge of the external surface of hydrotalcites are responsible for the reduction in humate concentrations. Nigro and O'Nieil [239], investigated the use of hydrotalcite in the removal of coloured impurities, such as ferrate, using different calcined hydrotalcite samples between 450 and 650 °C with their re-hydration in Bayer liquor. The calcination of hydrotalcite between 450 and 500 °C gave the greatest surface area and pore volume and the most effective hydrotalcite for removal of coloured impurity, indicating that adsorption was the predominate mechanism for ferrate removal.

Carbonate concentrations need to be minimal in Bayer liquors for the effective removal of impurity anions when using hydrotalcite or hydrocalumite. The high affinity of carbonate for the interlayer region prevents efficient intercalation of other anions. Grubbs and Valente [242], found that hydrotalcite could be formed without carbonate by reacting activated (calcined) magnesia with a sodium aluminate solution containing the anion in excess. Implementation of this process is limited as most impurities are not in excess. Studies by Perotta and Williams [243], found that the formation of hydrocalumite at temperatures up to 60 °C reduced the amount of oxalate in spent liquor, however, at higher temperatures tri-calcium aluminate (TCA – $3CaO\cdot Al_2O_3$) was the major product with no improvement in oxalate removal. Rosenberg et al. [244], discovered additives that helped stabilise the hydrocalumite structure, allowing a larger range of conditions that could be used in its formation without the undesirable formation of TCA occurring. Large-scale impurity removal is currently not feasible, due to the cost of recycling and recovering alumina from the LDH compounds.

4. Summary

Seawater neutralisation of bauxite refinery residues has been employed in recent years to reduce the pH and dissolved metal concentrations of wastewater, through the precipitation of hydrotalcite-like compounds and some other Mg, Ca, and Al hydroxide and carbonate minerals. These hydrotalcite-like compounds remove oxy-anions of transition metals through a combination of intercalation and adsorption of the anionic species on the external surfaces. Seawater neutralisation of bauxite refinery residues has beneficial consequences for red mud management. The reduced pH and soluble alkalinity eases handling and reuse, and dramatically reduces potential environmental impacts of red mud disposal.

Used in an appropriate way, layered double hydroxides offer a potential for new and efficient options for removal of impurities in aqueous solution, including alumina refinery liquor streams. The lamellar structure of LDHs can be used for the controlled addition or removal of a variety of species, both organic and inorganic. This is achieved through their ability to adjust the separation of the hydroxide layers, and the reactivity of the interlayer region. Hydrotalcite has a high selectivity for carbonate anions, making it ineffective as an anion-exchange material unless further treatment is made. Heating to 300 °C causes decarboxylation as the carbonate anion decomposes, resulting in an amorphous material that will absorb anions and return to its original hydrotalcite structure.

Acknowledgements

The financial and infra-structure support of the Queensland Research and Development Centre (QRDC-Alcan) and the Queensland University ofTechnology Inorganic Materials Research Program of the School of Physical and Chemical Sciences is gratefully acknowledged. One of the authors (SJP) is grateful to Alcan for a Masters scholarship.

References

[1] A.R. Hind, S.K. Bhargava, S.C. Grocott, Colloids Surf. A: Physicochem. Eng. Aspects 146 (1999) 359.
[2] M. Jamialahmadi, H. Muller-Steinhagen, J. Min. Met. Mater. Soc. (1998) 44.
[3] D. Chvedov, S. Ostap, T. Le, Colloids Surf. A: Physicochem. Eng. Aspects 182 (2001) 131.
[4] K. Komnitsas, G. Bartzas, I. Paspaliaris, Min. Eng. Process. Disp. Min. Ind. Waste 17 (2004) 183.
[5] H. Genc, J.C. Tjell, D. McConchie, O. Schuiling, J. Colloid Interface Sci. 264 (2003) 327.
[6] C. Lin, G. Maddocks, J. Lin, G. Lancaster, C. Chu, Aust. J. Soil Res. 42 (2004) 649.
[7] N.W. Menzies, I.M. Fulton, W.J. Morrell, J. Environ. Qual. 33 (2004) 1877.
[8] R.N. Summers, J.D. Pech, Agric. Ecosyst. Environ. 64 (1997) 219.

[9] The Guidelines, Australian and New Zealand Environment and Conservation Council (ANZEXX) and Agriculture and Resource Management Council of Australia and New Zealand (ARMCANZ) 1 (4) (2000), (Chapters 1–7).
[10] D.J. Glenister, M.R. Thornberg, Chemica 85 (1985) 100.
[11] C. Hanahan, D. McConchie, J. Pohl, R. Creelman, M. Clark, C. Stocksiek, Environ. Eng. Sci. 21 (2004) 125.
[12] H.S. Altundogan, S. Altundogan, F. Tumen, M. Bildik, Waste Manage. 22 (2002) 357.
[13] C. Brunori, C. Cremisini, L. D'Annibale, P. Massanisso, V. Pinto, Anal. Bioanal. Chem. 381 (2005) 1347.
[14] C. Lin, M.W. Clark, D.M. McConchie, G. Lancaster, N. Ward, Aust. J. Soil Res. 40 (2002) 805.
[15] C.-X. Lin, X.-X. Long, S.-J. Xu, C.-X. Chu, S.-Z. Mai, D. Jiang, Pedosphere 14 (2004) 371.
[16] E. Lombi, F.-J. Zhao, G. Wieshammer, G. Zhang, P. McGrath Steve, Environ. Pollut. 118 (2002) 445.
[17] B. Diaz, S. Joiret, M. Keddam, X.R. Novoa, M.C. Perez, H. Takenouti, Electrochem. Methods Corros. Res. 49 (2004) 3039.
[18] E. Lopez, B. Soto, M. Arias, A. Nunez, D. Rubinos, T. Barral, Water Res. 32 (1998) 1314.
[19] L. Santona, P. Castaldi, P. Melis, J. Hazard. Mater. 136 (2006) 324.
[20] D.J. Glenister, Chemica 85 (1985) 100.
[21] B.I. Whittington, Hydrometallurgy 43 (1996) 13.
[22] K. Solymar, J. Zoldi, T. Ferenczi, Mag. Alum. 26 (1989) 20.
[23] K. Solymar, I. Sajo, J. Steiner, J. Zoldi, Light Met. (1992) 209.
[24] S. Prakash, Z. Horvath, Publ. Tech. Univ. Heavy Ind. Ser. B: Metall. 34 (1979) 43.
[25] I. Paspaliaris, A. Karalis, Light Met. (1993) 35.
[26] R.M. Cornell, U. Schwertmann, The Iron Oxides, Second ed., Wiley-VCH, Weinheim, 2000.
[27] P.H. Hsu, G. Marion, Soil Sci. 140 (1985) 344.
[28] D. Langmuir, Gibbs Free Energies of Substances in the System Fe─O_2═H_2O─CO_2 at 25 °C, USA, 1969, p. 180.
[29] W.L. Lindsay, Chemical Equilibria in Soils, John Wiley Sons, New York, 1979, p. 449.
[30] P. Schindler, Chimia 17 (1963) 313.
[31] P. Basu, Light Min. (1983) 83.
[32] I.I. Diakonov, J. Schott, F. Martin, J.C. Harrichourry, J. Escalier, Geochimica et Cosmochimica Acta 63 (1999) 2247.
[33] K. Ishikawa, T. Yoshioka, T. Sato, A. Okuwaki, Hydrometallurgy 45 (1997) 129.
[34] F.J. Micale, D. Kiernan, A.C. Zettlemoyer, J. Colloid Interface Sci. 105 (1985) 570.
[35] Y. Hotta, S. Ozeki, T. Suzuki, J. Imai, K. Kaneko, Langmuir 7 (1991) 2649.
[36] V. Barron, J. Torrent, J. Colloid Interface Sci. 177 (1996) 407.
[37] T. Hiemstra, J.C.M. De Wit, W.H. Van Riemsdijk, J. Colloid Interface Sci. 133 (1989) 105.
[38] T. Hiemstra, W.H. van Riemsdijk, J. Colloid Interface Sci. 179 (1996) 488.
[39] D.G. Lewis, V.C. Farmer, Clay Min. 21 (1986) 93.
[40] J.D. Russell, R.L. Parfitt, A.R. Fraser, V.C. Farmer, Nature 248 (1974) 220.
[41] L. Charlet, A.A. Manceau, J. Colloid Interface Sci. 148 (1992) 443.
[42] L. Sigg, W. Stumm, Colloids Surf. 2 (1981) 101.
[43] D.D. Hansmann, M.A. Anderson, Environ. Sci. Technol. 19 (1985) 544.
[44] D.E. Yates, T.W. Healy, J. Colloid Interface Sci. 52 (1975) 222.
[45] S.H.R. Davies, J.J. Morgan, J. Colloid Interface Sci. 129 (1989) 63.
[46] A. Bibak, O.K. Borggaard, Soil Sci. 158 (1994) 323.
[47] F.J. Hingston, A.M. Posner, J.P. Quirk, J. Soil Sci. 25 (1974) 16.
[48] N.G. Holm, M.J. Dowler, T. Wadsten, G. Arrhenius, Geochimica et Cosmochimica Acta 47 (1983) 1465.
[49] R.M. McKenzie, J. Soil Res. 21 (1983) 505.
[50] K. Mesuere, W. Fish, Environ. Sci. Technol. 26 (1992) 2357.
[51] R.L. Parfitt, J.D. Russell, J. Soil Sci. 28 (1977) 297.
[52] R.L. Parfitt, R.S.C. Smart, J. Chem. Soc. Faraday Trans. 1: Phys. Chem. Conden. Phases 73 (1977) 796.
[53] E.D. Reyes, J.J. Jurinak, Soil Sci. Soc. Am. Proc. 31 (1967) 637.
[54] R.P.J.J. Rietra, T. Hiemstra, W.H. Van Riemsduk, Geochimica et Cosmochimica Acta 63 (1999) 3009.
[55] F.J. Hingston, R.J. Atkinson, A.M. Posner, J.P. Quirk, Specific adsorption of anions on anions on goethite, in: 9th International Congress of Soil Science, vol. 1, 1968, p. 669.
[56] G.W. Bruemmer, J. Gerth, K.G. Tiller, J. Soil Sci. 39 (1988) 37.
[57] L. Loevgren, Geochimica et Cosmochimica Acta 55 (1991) 3639.
[58] L. Loevgren, S. Sjoeberg, P.W. Schindler, Geochimica et Cosmochimica Acta 54 (1990) 1301.
[59] B. Whittington, T. Fallows, Hydrometallurgy 45 (1997) 289.
[60] B.I. Whittington, B.L. Fletcher, C. Talbot, Hydrometallurgy 49 (1998) 1.
[61] R.G. Breuer, L.R. Barsotti, A.C. Kelly, Behaviour of Silica in Sodium Solutions, Interscience, New York, 1963.
[62] J.J. Kote, Light Met. (1989) 45.
[63] H.D. Grundy, I. Hassan, Can. Mineral. 20 (1982) 239–251.
[64] G. Hermeler, J.C. Buhl, W. Hoffmann, Catal. Today 8 (1991) 415.
[65] M.G. Leiteizen, L.A. Pashkevich, I.B. Firfarova, D.I. Tsekhovol'skaya, Tsvetnye Metal. (1974) 21.
[66] S. Ostap, Hydrometallogy 15 (1985) 1411.
[67] R.G. Breuer, L.R. Barsotti, A.C. Kelly, Aluminum 1 (1963) 133.
[68] M.C. Barnes, J. Addai-Mensah, A.R. Gerson, Colloids Surf. A: Physicochem. Eng. Aspects 157 (1999) 101.
[69] T. Oku, K. Yamada, T. Harato, H. Kato, Environ. Sci. Technol. (1972) 4.
[70] V.L.P. Ni, G.L. Perekhrest, T.V. Solenko, Zhurnal Prikladnoi Khimii 37 (1964) 22.
[71] M.C. Barnes, J. Addai-Mensah, A.R. Gerson, Microporous and Mesoporous Mater. 31 (1999) 287.
[72] R.M. Barrer, J.F. Cole, H. Villiger, J. Chem. Soc. A: Inorg. (1970) 1523.
[73] N.S. Volkova, D.I. Tsekhovol'skaya, N.I. Eremin, Tsvetnye Metal. 44 (1971) 31.
[74] R.W.G. Wyckoff, Crystal Structures, vol. 1, Wiley, New York, 1963.
[75] K. Zheng, A.R. Gerson, J. Addai-Mensah, R.S.C. Smart, J. Cryst. Growth 171 (1997) 197.
[76] R. Apak, K. Guclu, M.H. Turgut, J. Colloid Interface Sci. 203 (1998) 122.
[77] J. Pradhan, J. Das, S. Das, R.S. Thakur, J. Colloid Interface Sci. 204 (1998) 169.
[78] R. Apak, G. Atun, K. Guclu, E. Tutem, G. Keskin, J. Nucl. Sci. Technol. 32 (1995) 1008.
[79] Y.G. Berube, P.L. De Bruyn, J. Colloid Interface Sci. 27 (1968) 305.
[80] A. Breeuwsma, J. Lyklema, J. Colloid Interface Sci. 43 (1973) 437.
[81] L.Y.L. Li, Colloids Surf. A: Physicochem. Eng. (1993) 298.
[82] H. Tamura, A. Tanaka, K.-y. Mita, R. Furuichi, J. Colloid Interface Sci. 209 (1999) 225.
[83] G. Sposito, Soil Sci. Soc. Am. J. 45 (1981) 292.
[84] G. Sposito, Environ. Sci. Technol. 32 (1998) 2815.
[85] H. Hohl, W. Stumm, J. Colloid Interface Sci. 55 (1976) 281.
[86] C.-P. Huang, W. Stumm, J. Colloid Interface Sci. 43 (1973) 409.
[87] L. Liang, J.J. Morgan, ACS Symp. Ser. 416 (1990) 293.
[88] C.K.D. Hsi, D. Langmuir, Geochimica et Cosmochimica Acta 49 (1985) 1931.
[89] D.G. Lumsdon, L.J. Evans, J. Colloid Interface Sci. 164 (1994) 119.
[90] G. Atun, G. Hisarli, J. Colloid Interface Sci. 228 (2000) 40.
[91] V. Gupta, M. Gupta, S. Sharma, Water Res. 35 (2001) 1125.
[92] C.A. Johnson, Geochimica et Cosmochimica Acta 50 (1986) 2433.
[93] S. Yariv, H. Cross, Geochemistry of Colloid Systems for Earth Scientists, Springer-Verlag, New York, 1979.
[94] V.K. Gupta, S. Sharma, Environ. Sci. Technol. 36 (2002) 3612.
[95] R.N. Summers, N.R. Guise, D.D. Smirk, Fertil. Res. 34 (1993) 85.
[96] D. McConchie, M. Clark, C. Hanahan, R. Fawkes, Min. Met. Mater. Soc. 1 (1999) 391.
[97] K.H. Lieser, Appl. Sci. 13 (1975) 91.
[98] V. Apak, E. Unseren, Floccul. Biotechnol. Sep. Syst. (1987) 765.
[99] J. Gregory, Appl. Sci. 27 (1978) 89.
[100] D. McConchie, P. Saenger, R. Fawkes, in: V.R.a.C.C. Nesbitt (Ed.), Second International Symposium on Extraction and Processing for the Treatment and Minimization of Wastes, The Minerals, Metals and Material Society, 1996, p. 407.

[101] J. Somes, N. Menzies, D. Mulligan, ASSSI National Soils Conference, Brisbane, QLD, 1998, p. 546.
[102] B. Koumanova, M. Drame, M. Popangelova, Resour. Conser. Recycl. 19 (1997) 11.
[103] E.E. Shannon, K.I. Verghese, J. Water Pollut. 48 (1976) 1948.
[104] G.A. Graham, R. Fawkes, Proceedings of the International Bauxsite Tailings Workshop, Perth, WA, Australia, 1992.
[105] M.B. McBride, Environmental Chemistry of Soils, Oxford University Press, New York, 1994.
[106] D. McConchie, M. Clark, C. Hanahan, F. Davies-McConchie, 3rd Queensland Environmental Conference: Sustainable Solutions for Industry and Government, Brisbane, QLD, Australia, 2000, p. 201.
[107] H.D. Smith, G.M. Parkinson, 7th International Alumina Quality Workshop, 2005.
[108] H.D. Smith, G.M. Parkinson, R.D. Hart, J. Cryst. Growth 275 (2005) 1665.
[109] K. Periasamy, C. Namasivayam, Ind. Eng. Chem. Res. 33 (1994) 317.
[110] H.S. Altundogan, S. Altundogan, F. Tumen, M. Bildik, Waste Manage. 20 (2000) 761.
[111] A.N. Ay, B. Zuemreoglu-Karan, A. Temel, Microporous Mesoporous Mater. 98 (2007) 1.
[112] J. Shibata, N. Murayama, K. Sakai, H. Yamamoto, World Congress of Chemical Engineering, 7th, Glasgow, United Kingdom, July 10–14, 2005.
[113] Y. Kiso, Y.J. Jung, T. Yamada, M. Nagai, K.S. Min, Water Sci. Technol.: Water Supply 5 (2005) 75.
[114] H. Hirahara, S. Aisawa, H. Sato, S. Takahashi, Y. Umetsu, E. Narita, Nendo Kagaku 45 (2005) 6.
[115] S. Peng, Y. Yang, T. Chen, S. Jiang, H.f. Xu, Guisuanyan Xuebao 33 (2005) 1023.
[116] N. Murayama, M. Tanabe, R. Shibata, H. Yamamoto, J. Shibata, Kagaku Kogaku Ronbunshu 31 (2005) 285.
[117] T. Murakami, H. Oshima, T. Kuwabara, T. Sato, A. Kawamoto, Mizu Kankyo Gakkaishi 28 (2005) 269.
[118] S. Yapar, P. Klahre, E. Klumpp, Turk. J. Eng. Environ. Sci. 28 (2004) 41.
[119] T. Kuwabara, T. Sato, T. Nonaka, H. Yamamoto, M. Aizaki, Y. Fukuda, Mizu Kankyo Gakkaishi 26 (2003) 423.
[120] J. Orthman, H.Y. Zhu, G.Q. Lu, Sep. Purif. Technol. 31 (2003) 53.
[121] Y.W. You, H.T. Zhao, G.F. Vance, Environ. Technol. 22 (2001) 1447.
[122] H.Y. Zhu, J. Orthman, G.Q. Lu, Proceedings of the Asia-Pacific Conference, 3rd, Hong Kong, China, December, 2001, p. 356.
[123] M.A. Ulibarri, I. Pavlovic, C. Barriga, M.C. Hermosin, J. Cornejo, Appl. Clay Sci. 18 (2001) 17.
[124] U. Costantino, F. Marmottini, M. Nocchetti, R. Vivani, Eur. J. Inorg. Chem. (1998) 1439.
[125] R.L. Frost, M.L. Weier, M.E. Clissold, P.A. Williams, J.T. Kloprogge, Thermochimica Acta 407 (2003) 1.
[126] T. Lopez, P. Bosch, E. Ramos, R. Gomez, O. Novaro, D. Acosta, F. Figueras, Langmuir 12 (1996) 189.
[127] A.I. Khan, D. O'Hare, J. Mater. Chem. 12 (2002) 3191.
[128] M.C. Van Oosterwyck-Gastuche, G. Brown, M.M. Mortland, Clay Min. 7 (1967) 177.
[129] M.R. Weir, J. Moore, R.A. Kydd, Chem. Mater. 9 (1997) 1686-.
[130] S. Miyata, Clays Clay Min. 28 (1980) 50.
[131] A.V. Radha, P. Vishnu Kamath, C. Shivakumara, Solid State Sci. 7 (2005) 1180.
[132] F. Trifiro, A. Vaccari, in: J.L. Atwood, J.E.D. Davies, D.D. MacNicol, F. Vogtle, J.M. Lehn, G. Alberti, T. Bein (Eds.), Comprehensive Supramolecular Chemistry, Solid-State Supramolecular Chemistry: Two- and Three-Dimensional Inorganic Networks, Pergamon, Oxford, 1996, p. 251.
[133] E.L. Crepaldi, P.C. Pavan, J.B. Valim, J. Brazil. Chem. Soc. 11 (2000) 64.
[134] L. Pesic, S. Salipurovic, V. Markovic, D. Vucelic, W. Kagunya, W. Jones, J. Mater. Chem. 2 (1992) 1069.
[135] V. Rives, Layered Double Hydroxides: Present and Future, Nova Science, New York, 2001.
[136] H.F.W. Taylor, Mineral. Mag. 39 (1973) 377.
[137] G. Marcelin, N.J. Stockhausen, J.F.M. Post, A. Schutz, J. Phys. Chem. 93 (1989) 4646.
[138] S. Miyata, Clays Clay Min. 23 (1975) 369.
[139] D.L. Bish, Bull. de Mineralogie 103 (1980) 170.
[140] G.W. Brindley, S. Kikkawa, Am. Mineral. 64 (1979) 836.
[141] G.W. Brindley, S. Kikkawa, Clays Clay Min. 28 (1980) 87.
[142] E.H. Nickel, R.M. Clarke, Am. Mineral. 61 (1976) 366.
[143] P.G. Rouxhet, H.F.W. Taylor, Chimia 23 (1969) 480.
[144] R.L. Frost, M.L. Weier, M.E. Clissold, P.A. Williams, Spectrochim. Acta Part A: Mol. Biomol. Spectrosc. 59 (2003) 3313.
[145] R.L. Frost, W. Martens, Z. Ding, J.T. Kloprogge, T.E. Johnson, Spectrochim. Acta A 59 (2003) 291.
[146] R.L. Frost, Z. Ding, W.N. Martens, T.E. Johnson, J.T. Kloprogge, Spectrochim. Acta Part A: Mol. Biomol. Spectrosc. 59 (2003) 321.
[147] A. Tsujimura, M. Uchida, A. Okuwaki, J. Hazard. Mater. 143 (2007) 582.
[148] G.-J. Guo, P.-H. Ma, M.-X. Chu, Huaxue Xuebao 62 (2004) 2150.
[149] Z.P. Xu, H.C. Zeng, Chem. Mater. 13 (2001) 4564.
[150] R.L. Frost, A.W. Musumeci, M.O. Adebajo, W. Martens, J. Therm. Anal. Calorim. 89 (2007) 95–99.
[151] R.L. Frost, A.W. Musumeci, J.T. Kloprogge, M.O. Adebajo, W.N. Martens, J. Raman Spectrosc. 37 (2006) 733.
[152] X. Duan, D. Li, L. Shi, T. Feng, Mizu Kankyo Gakkaishi (2004) 7.
[153] R.L. Frost, A.W. Musumeci, T. Bostrom, M.O. Adebajo, M.L. Weier, W. Martens, Thermochim. Acta 429 (2005) 179.
[154] E.D. Dimotakis, T.J. Pinnavaia, Inorg. Chem. 29 (1990) 2393.
[155] G.R. Williams, A.J. Norquist, D. O'Hare, Chem. Mater. 16 (2004) 975.
[156] S.K. Yun, T.J. Pinnavaia, Inorg. Chem. 35 (1996) 6853.
[157] A. De Roy, C. Forano, K. El Malki, J.P. Besse, Synth. Microporous Mater. 2 (1992) 108.
[158] W.T. Reichle, Solid State Ionics 22 (1986) 135.
[159] R.L. Frost, A.W. Musumeci, J. Colloid Interface Sci. 302 (2006) 203.
[160] J.T. Kloprogge, L. Hickey, R. Trujillano, M.J. Holgado, M.S. San Roman, V. Rives, W.N. Martens, R.L. Frost, Cryst. Growth Des. 6 (2006) 1533.
[161] K.L. Erickson, T.E. Bostrom, R.L. Frost, Mater. Lett. 59 (2005) 226.
[162] H.P. Boehm, J. Steinle, C. Vieweger, Angew. Chem. 89 (1977) 259.
[163] L. Indira, M. Dixit, P.V. Kamath, J. Power Sources 52 (1994) 93–97.
[164] L. Indira, P.V. Kamath, J. Mater. Chem. 4 (1994) 1487.
[165] M. Lal, A.T. Howe, J. Solid State Chem. 39 (1981) 368.
[166] B.G. Ahn, S.J. Jung, M.R. Kang, K.J. Kim, H.M. Lim, J.H. Nam, Mizu Kankyo Gakkaishi (2005) 55.
[167] J. Das, B.S. Patra, N. Baliarsingh, K.M. Parida, Appl. Clay Sci. 32 (2006) 252.
[168] M. Liu, J.J. Yang, G.Q. Wu, L.Y. Wang, Wuji Huaxue Xuebao 22 (2006) 1771.
[169] S.V. Prasanna, R.A.P. Rao, P.V. Kamath, J. Colloid Interface Sci. 304 (2006) 292.
[170] M. Uehara, A. Yamzaki, T. Umezawa, K. Takahashi, S. Tsutsumi, Clays Clay Min. 47 (1999) 726.
[171] T.J. Pinnavaia, Science 220 (1983) 365.
[172] S. Carlino, Solid State Ionics 98 (1997) 73.
[173] S.P. Newman, W. Jones, N. J. Chem. 22 (1998) 105.
[174] Y. Hu, P.K. Davies, Mater. Sci. Forum 152–153 (1994) 277.
[175] F. Kooli, M.J. Holgado, V. Rives, S. Sanroman, M.A. Ulibarri, Mater. Res. Bull. 32 (1997) 977.
[176] N. Mikami, M. Sasaki, S. Horibe, T. Yasunaga, J. Phys. Chem. 88 (1984) 1716.
[177] M. Sasaki, N. Mikami, T. Ikeda, K. Hachiya, T. Yasunaga, J. Phys. Chem. 86 (1982) 4413.
[178] T. Hibino, A. Tsunashima, Chem. Mater. 9 (1997) 2082.
[179] F. Kooli, W. Jones, V. Rives, M.A. Ulibarri, J. Mater. Sci. Lett. 16 (1997) 27.
[180] E.M. Serwicka, P. Nowak, K. Bahranowski, W. Jones, F. Kooli, J. Mater. Chem. 7 (1997) 1937.
[181] F. Kooli, V. Rives, M.A. Ulibarri, Inorg. Chem. 34 (1995) 5114.
[182] M. Figlarz, B. Gerand, A. Delahaye-Vidal, B. Dumont, F. Harb, A. Coucou, F. Fievet, Solid State Ionics 43 (1990) 143.
[183] S. Miyata, Clays Clay Min. 31 (1983) 305.
[184] P.K. Dutta, M. Puri, J. Phys. Chem. 93 (1989) 376.
[185] L.M. Parker, N.B. Milestone, R.H. Newman, Ind. Eng. Chem. Prod. Res. Develop. 34 (1995) 1196.

[186] T. Stanimirova, G. Kirov, Geologiya 92 (2000) 121.
[187] H. Kaatuzian, A. Rostami, A. Ajdarzadeh Oskouei, J. Optics B 7 (2005) 157.
[188] N. Sui, J. Hu, J. Chen, P. Kuang, D. Joyce, J. Psychopharmacol. 15 (2001) 287.
[189] S.K. Zhang, P.V. Santos, R. Hey, A. Garcia-Cristobal, A. Cantarero, Appl. Phys. Lett. 77 (2000) 4380.
[190] H.-S. Shin, M.-J. Kim, S.-Y. Nam, H.-C. Moon, Water Sci. Technol. 34 (1996) 161.
[191] T.S. Stanimirova, G. Kirov, E. Dinolova, J. Mater. Sci. Lett. 20 (2001) 453.
[192] W.T. Reichle, S.Y. Kang, D.S. Everhardt, J. Catal. 101 (1986) 352.
[193] T. Sato, T. Wakabayashi, M. Shimada, Ind. Eng. Chem. Prod. Res. Develop. 25 (1986) 89.
[194] R.L. Frost, A.W. Musumeci, J.T. Kloprogge, M.O. Adebajo, W.N. Martens, J. Raman Spectrosc. 37 (7) (2006) 733.
[195] R.L. Frost, A.W. Musumeci, W.N. Martens, M.O. Adebaj, J. Bouzaid, J. Raman Spectrosc. 36 (10) (2005) 925.
[196] R.L. Frost, M.L. Weier, J.T. Kloprogge, J. Raman Spectrosc. 34 (10) (2003) 760.
[197] T.N. Moroz, D.K. Arkhipenko, Geologiya i Geofizika 2 (1991) 58.
[198] J.T. Kloprogge, R.L. Frost, in: V. Rives (Ed.), Layered Double Hydroxides: Present and Future, Nova Science, New York, 2001.
[199] W. Kagunya, R. Baddour-Hadjean, F. Kooli, W. Jones, Chem. Phys. 236 (1998) 225.
[200] M. Jose dos Reis, F. Silverio, J. Tronto, J.B. Valim, J. Phys. Chem. Solids 65 (2004) 487.
[201] J. Perez-Ramirez, G. Mul, J.A. Moulijn, Vib. Spectrosc. 27 (2001) 75.
[202] D.L. Bish, G.W. Brindley, Am. Mineral. 62 (1977) 458.
[203] M.K. Titulaer, J.B.H. Jansen, J.W. Geus, Clays Clay Min. 42 (1994) 249.
[204] F.A. Mumpton, H.W. Jaffe, C.S. Thompson, Am. Mineral. 50 (1965) 1893.
[205] L. Chatelet, J.Y. Bottero, J. Yvon, A. Bouchelaghem, Colloids Surf. A: Physicochem. Eng. Aspects 111 (1996) 167.
[206] T. Lopez, P. Bosch, M. Asomoza, R. Gomez, E. Ramos, Mater. Lett. 31 (1997) 311.
[207] F.M. Labajos, V. Rives, M.A. Ulibarri, J. Mater. Sci. 27 (1992) 1546.
[208] M. Valcheva-Traykova, N. Davidova, A. Weiss, J. Mater. Sci. 28 (1993) 2157.
[209] J.T. Kloprogge, R.L. Frost, J. Solid State Chem. 146 (1999) 506.
[210] J. Perez-Ramirez, G. Mul, F. Kapteijn, J.A. Moulijn, J. Mater. Chem. 11 (2001) 2529.
[211] J.T. Kloprogge, L. Hickey, R.L. Frost, J. Raman Spectrosc. 35 (2004) 967.
[212] J.T. Kloprogge, D. Wharton, L. Hickey, R.L. Frost, Am. Mineral. 87 (2002) 623.
[213] V.C. Farmer (Ed.), Mineralogical Society Monograph 4: The Infrared Spectra of Minerals, 1974.
[214] K. Nakamoto (Ed.), Infrared and Raman Spectra of Inorganic and Coordination Compounds. Part A: Theory and Applications in Inorganic Chemistry, 5th ed., 1997.
[215] C. Barriga, F. Kooli, V. Rives, M.A. Ulibarri, H. Kessler (Eds.), Marcel Dekker, New York, 1996, p. 661.
[216] O. Clause, M. Gazzano, F. Trifiro, A. Vaccari, L. Zatorski, Appl. Catal. 73 (1991) 217.
[217] L. Hickey, J.T. Kloprogge, R.L. Frost, J. Mater. Sci. 35 (2000) 4347.
[218] J.I. Di Cosimo, V.K. Diez, M. Xu, E. Iglesia, C.R. Apesteguia, J. Catal. 178 (1998) 499.
[219] C. Morterra, G. Ghiotti, F. Boccuzzi, S. Coluccia, J. Catal. 51 (1978) 299.
[220] R. Philipp, K. Fujimoto, J. Phys. Chem. 96 (1992) 9035.
[221] R.L. Frost, K.L. Erickson, J. Therm. Anal. Calorim. 76 (2004) 217.
[222] T. Lopez, E. Ramos, P. Bosch, M. Asomoza, R. Gomez, Mater. Lett. 30 (1997) 279.
[223] F. Malherbe, J.-P. Besse, J. Solid State Chem. 155 (2000) 332.
[224] D. Tichit, M.H. Lhouty, A. Guida, B.H. Chiche, F. Figueras, A. Auroux, D. Bartalini, E. Garrone, J. Catal. 151 (1995) 50.
[225] O. Marino, G. Mascolo, Thermochim. Acta 55 (1982) 377.
[226] G. Mascolo, O. Marino, Mineral. Mag. 43 (1980) 619.
[227] G. Brown, G.W. Brindley, Mineral. Soc. Monogr. 5 (1980) 305.
[228] G.W. Brindley, G. Brown (Eds.), Mineralogical Society Monograph No. 5: Crystal Structures of Clay Minerals and Their X-ray Identification, 1980.
[229] D.M. Moore, R.C. Reynolds, X-ray Diffraction and the Identification and Analysis of Clay Minerals, 2nd ed., 1997.
[230] J. Thorez, Practical Identification of Clay Minerals: A Handbook for Teachers and Students in Clay Mineralology, Belgium State University Press, Dison, Lelotte, 1976.
[231] D.M. Moore, R.C. Reynolds, X-ray Diffraction and the Identification and Analysis of Clay Minerals, 2nd ed., Oxford University Press, New York, 1997.
[232] A. Vaccari, Catal. Today 41 (1998) 53.
[233] W.T. Reichle, ChemTech 16 (1986) 58.
[234] H.D. Ruan, R.L. Frost, J.T. Kloprogge, L. Duong, Spectrochim. Acta Part A: Mol. Biomol. Spectrosc. 58A (2002) 265.
[235] S. Miyata, T. Kumura, Chem. Lett. 8 (1973) 843.
[236] F. Kooli, I. Crespo, C. Barriga, M.A. Ulibarri, V. Rives, J. Mater. Chem. 6 (1996) 1199.
[237] S. Misra, Adsorbent and substrate products and method of producing the same, US Patent 4656156, (1987).
[238] S. Misra, Synthetic hydrotalcite. US Patent 6846870, (1990).
[239] W.A. Nigro, G.A. O'Neil, Method for reducing the amount of colorants in a caustic liquor, US Patent 5068095, (1991).
[240] R.B. Phillips, N.M. Fitzgerald, B.L. McCormick, Method for improving the brightness of aluminium hydroxide. US Patent 5624646, (1997).
[241] B. Schepers, G. Bayer, E. Urmann, K. Schanz, Method for removing harmful organic compounds from aluminate liquors of the Bayer process, US Patent 4046855, (1977).
[242] D.K. Grubbs, P.E. Valente, Direct synthesis of anion substituted hydrotalcite, US Patent 5362457, (1994).
[243] A.J. Perrotta, F. Williams, Light Met. (1995) 77.
[244] S.P. Rosenberg, D.J. Wilson, C.A. Heath, Light Met. (2000) 53.